ON THE CLUSTER PHYSICS OF SUNYAEV-ZEL'DOVICH SURVEYS I:
THE INFLUENCE OF FEEDBACK, NON-THERMAL PRESSURE AND CLUSTER SHAPES ON Y-M SCALING RELATIONS

N. BATTAGLIA[1,2,3], J. R. BOND[2], C. PFROMMER[4,2], J. L. SIEVERS[2,5]

[1] Department of Astronomy and Astrophysics, University of Toronto, 50 St George, Toronto ON, Canada, M5S 3H4
[2] Canadian Institute for Theoretical Astrophysics, 60 St George, Toronto ON, Canada, M5S 3H8
[3] McWilliams Center for Cosmology, Carnegie Mellon University, Department of Physics, 5000 Forbes Ave., Pittsburgh PA, USA, 15213
[4] Heidelberg Institute for Theoretical Studies, Schloss-Wolfsbrunnenweg 35, D-69118 Heidelberg, Germany
[5] Joseph Henry Laboratories of Physics, Jadwin Hall, Princeton University, Princeton NJ, USA, 08544
Submitted to ApJ

ABSTRACT

The utility of large Sunyaev Zel'dovich (SZ) surveys for determining cosmological parameters from cluster abundances is limited by the theoretical uncertainties in the integrated SZ-flux-to-mass relation, Y-M. We explore how non-thermal pressure and the anisotropic shape of the gas distribution of the intracluster medium (ICM) impacts Y-M scaling using a suite of hydrodynamical TreePM-SPH simulations of the cosmic web in large periodic boxes. We contrast results for models with different treatments of entropy injection and transport, varying radiative cooling, star formation and accompanying supernova feedback, cosmic rays, and energetic feedback from active galactic nuclei (AGN) and/or starbursts. We find that the gas kinetic-to-thermal pressure ratio from internal bulk motions depends on the cluster mass, and increases in the outer-cluster due to enhanced substructure, as does the asphericity of the ICM gas (which is substantially more pronounced for the dark matter). The asphericity is less dependent on the mass and on variations in the simulated physics. With only a $\sim 5-10\%$ correction to projected (observable) ellipticities, we can infer the 3D ellipticities. We find radii around R_{500} – within which the mean density is 500 times the critical density – are the most robust for studying virial properties of clusters, being far enough out to avoid the complex "short-distance" physics of the cluster core, having a relatively low non-thermal to thermal pressure ratio ($\sim 20\%$), and having the smallest variance of gas ellipticity as cluster mass and redshift vary. Our simulated Y-M-slope roughly follows the self-similar $Y \sim M^{5/3}$ prediction, except for a steepening due to a deficit of gas in lower mass clusters at low redshift in our AGN-feedback simulations. The overall Y-M amplitudes with AGN feedback and radiative cooling are lower than for the shock-heating-only case, by $\sim 30\%$. AGN feedback enhances slightly the overall Y-M-scatter, from $\sim 11\%$ to $\sim 13\%$, a reflection of accretion history variations due to cluster merging. The scatter falls back to $\sim 11\%$ if we select clusters with lower kinetic pressure. If we split the cluster system into lower, middle and upper bands of $P_{\rm kin}/P_{\rm th}$, we find a $\sim 10\%$ effect on Y-M. A 3-split on asymmetry as measured by the long-to-short axis ratio has a $< 10\%$ effect on Y-M, but using 3D-sphericalized estimates instead of projected (cylindrical) has a a $\sim 30\%$ effect. Identifying observable second parameters related to internal bulk flows and anisotropy for cluster-selection to minimize Y-M-scatter in a (fuzzy) "fundamental plane" would allow tighter cosmological parameter constraints.

Subject headings: Cosmic Microwave Background — Cosmology: Theory — Galaxies: Clusters: General — Large-Scale Structure of Universe — Methods: Numerical

1. INTRODUCTION

Clusters are the largest gravitationally-collapsed objects in the universe, forming at sites of constructive interference of long waves in the primordial density fluctuations, the coherent peak-patches (Bardeen et al. 1986; Bond & Myers 1996). The interiors are separated from the Hubble-flow, but maintain contact with the nearby cosmic web through ongoing accretion and mergers as they evolve. Although there is a strong internal baryon-to-dark-matter density bias, a consequence of collisional-to-collisionless physics, when cluster-scale-averaged the smoothed densities are nearly in the universal Hubble-volume-smoothed proportion. Clusters have proven to be useful cosmological probes as the rarest collapsed-event tracers of the growth of structure in the universe, with a well-defined number count that steeply falls as mass and redshift increase. The number density tail is very sensitive to changes in cosmological parameters and primordial non-Gaussianity. In clusters most of the baryons are in the form of a hot diffuse plasma, the intracluster medium (ICM). The remaining baryons

are housed in the cluster's numerous stars and galaxies. Observations of gas in the cluster system not only reveal the detailed astrophysical processes at work in the ICM, but the counts derived as a function of the global-cluster-observables such as thermal energy content can allow for a high precision probe of the cosmological parameters defining the count density shape and amplitude.

This scheme of using the cluster system for cosmology must rely on simulations capturing the physics at work: the clusters have been revealed to be too complex for simple sphericalized analytical modelling as the observations have been progressively refined and resolutions improved. We hope that the basic global observables will be sufficiently robust to the high resolution complexities that the cluster/group system can be cosmologically useful, but that must be demonstrated by detailed theoretical work with a necessarily heavy computational component. Direct observation of mass or gravitational energy or overall binding energy of clusters would be ideal, but we are stuck with what can be observed, in the optical, X-ray and microwave/radio/sub-mm. Each derived observable from these

windows into clusters is fraught with complication that requires a computational understanding. A thermal Sunyaev-Zel'dovich (SZ) (Sunyaev & Zeldovich 1970) probe directly observes the integrated Compton-y parameter which is a measure of the cluster's global gas heat-energy content, a volume-average of the thermal gas pressure, and this is related to gravitational energy through the virial relation, so it might be expected to provide a robust probe. In this paper, and the following sequence, BBPS2,3,4 (Battaglia et al. 2011a,b,c), a follow-on to (Battaglia et al. 2010), we focus on the SZ effect, the Compton up-scattering of cosmic microwave background (CMB) photons by hot electrons with its unique signature of a spatially-varying distortion of the CMB spectrum, a decrement in thermodynamic temperature at frequencies below $\sim 220\,\mathrm{GHz}$, and an excess above. The SZ signal is proportional to the integrated electron pressure, so the hot gas of the ICM dominates the effect. The SZ surface brightness is independent of the redshift a specific cluster is at. Hence SZ surveys have a different selection function in redshift and in mass than X-ray and optical cluster surveys do, being generically more sensitive to higher redshift clusters. The combination of the three probes can provide more robust, tighter constraints on cosmological parameters than any one can alone.

In a large cluster survey there is a wealth of information contained on cosmology and structure formation. The abundance of clusters, their distribution in redshift, and their spatial clustering should be determined purely by the geometry of the universe, the power spectrum of initial density fluctuations, and cosmological parameters such as the *rms* amplitude of the (linear) density power spectrum on cluster-mass scales, σ_8, the mass-energy density in baryons, dark matter, and dark energy, and the equation of state of the latter. In SZ surveys, the number counts as a function of the total SZ flux (integrated Compton-y parameter Y) and redshift and the angular power spectrum are two complementary probes of cosmology (e.g., Birkinshaw 1999; Carlstrom et al. 2002). Identifying clusters through blind SZ surveys and measuring their integrated power spectrum have been long term goals in CMB research, and are reaching fruition through, *e.g.*, the South Pole Telescope, SPT (e.g., Lueker et al. 2010; Shirokoff et al. 2010; Keisler et al. 2011; Vanderlinde et al. 2010), the Atacama Cosmology Telescope, ACT (e.g., Fowler et al. 2010; Dunkley et al. 2010; Marriage et al. 2010), and the *Planck* satellite (e.g., Planck Collaboration et al. 2011b,c,a). To determine cosmological parameters from number counts requires understanding the relationship of SZ observables such as total SZ flux to fundamental cluster properties such as mass M. And to determine them from the SZ power spectrum requires knowing the sum of the squares of pressure profiles of unresolved groups and clusters, as well as of resolved ones, weighted by the counts. Both depend sensitively on σ_8, hence can provide an independent measure of it. Such extraction from the SZ probes is inevitably entangled with the uncertainties in the astrophysical properties of the ICM. This paper deconstructs the influence of various physical processes on the Y-M scaling relation. BBPS2 does the same for the SZ power spectrum.

Previous work attempted to calibrate the Y-M scaling relation through observations (e.g., Benson et al. 2004; Bonamente et al. 2008; Marrone et al. 2009; Andersson et al. 2010; Sayers et al. 2011; Marrone et al. 2011), self-calibration techniques (e.g., Majumdar & Mohr 2003, 2004; Lima & Hu 2004; Chaudhuri & Majumdar 2011; Nath & Majumdar 2011), simulations (e.g., da Silva et al. 2004; Motl et al. 2005; Schäfer et al. 2006a,b; Bonaldi et al. 2007) and analytical ap-

proaches (Bode et al. 2007; Shaw et al. 2008; Mroczkowski 2011). Combining Y-M scaling relations so determined with the survey selection function and marginalizing over associated statistical and systematic uncertainties can enable accurate determination of cosmological parameters. Using a small sample of SZ-clusters, SPT (Vanderlinde et al. 2010) and ACT (Sehgal et al. 2011) determined some cosmological constraints, e.g., on σ_8. However, the errors on σ_8 are dominated by systematic uncertainties in the underlying cluster physics, making this approach not competitive with other cosmological probes. Hence in order to improve upon the determination of cosmological parameters, a better understanding of the mass proxies and their scatter is needed (Nagai 2006; Shaw et al. 2008; Stanek et al. 2010; Yang et al. 2010; Krause et al. 2011).

1.1. ICM processes

Clusters have been increasingly revealed to be complex systems as the data has progressively improved, necessitating a revision of the simplified pictures popular in the eighties for interpreting the data. For example, pioneering work by Kaiser (1986) assumed that clusters were self-similar systems with the mass determining their ICM thermodynamic properties. As shown by subsequent X-ray observations, this self-similar description is broken, especially on group scales; low-mass systems are less luminous in comparison to the self-similar expectation (see Voit 2005, for a review). Studying how non-thermal processes such as magnetic fields, cosmic rays, active galactic nuclei (AGN), star formation, radiative cooling and bulk motions contribute to the energy balance and thermodynamic stability within clusters is a very active research field. It remains unclear how these processes vary with cluster radius or dynamical state. State-of-the-art simulations are about the only tool available for building a consistent picture of clusters. Here we contribute to these non-thermal studies by using our simulations to explore the three effects that influence the Y-M scaling relation. These are the feedback processes that appear to be necessary to explain the thermodynamic characteristics of the ICM and avoid a cooling catastrophe leading to too much star formation, non-thermal pressure support from bulk motions internal to the clusters that are a natural consequence of a dynamically evolving structure formation hierarchy, and deviations from spherical symmetry.

1.2. Energetic feedback

In many clusters the ICM cooling times are much shorter than a Hubble time (Fabian 1994; Cavagnolo et al. 2009), which should cause extremely high star formation rates that are well beyond what is observed. However, current simulations with *only* radiative cooling and star formation excessively over-cool cluster centers (e.g., Suginohara & Ostriker 1998; Lewis et al. 2000; Pearce et al. 2000), even with the addition of supernova feedback. This leads to too many stars in the cluster cores, an unphysical rearrangement of the thermal and hydrodynamic structure, and creates problems when comparing simulations to observations, in particular for the entropy and pressure profiles. Self-regulated, inhomogeneous energy feedback mechanisms by, e.g., AGN are very successful in globally stabilizing the group and cluster "atmospheres", and, in particular, preventing the cooling catastrophe (Churazov et al. 2001). Observations of cool core galaxy clusters show evidence for AGN-moderation of the cooling and AGN feedback can potentially heat the surrounding ICM from kpc sized bubbles to hundreds of kpc sized outbursts (McNamara et al. 2005).

In hydrodynamical simulations, it has been shown that incorporating a sub-grid for AGN feedback can resolve the overcooling problem (e.g., Sijacki et al. 2007, 2008; Battaglia et al. 2010; McCarthy et al. 2011). The effects of AGN feedback on the ICM will mainly alter the cluster and group cores, where the actual physics is poorly resolved and understood. These effects can seen to be dramatic in X-ray observations (e.g., Fabian et al. 2003), since the emission is proportional to gas density squared. Since the SZ signal is proportional to the gas pressure, these effects are smaller. Hence, AGN feedback should only perturb the integrated thermal SZ signal, with an amplitude that is not yet known.

1.3. Non-thermal pressure support

Studying non-thermal pressure support from bulk motion in clusters has a long history and was first noticed in simulations by Evrard (1990), who showed that estimates for the binding mass of a cluster using a hydrostatic isothermal β-model in comparison to a fit to the surface brightness profile differed by 15%. They found that inclusion of velocity dispersion in the hydrostatic isothermal β-model reconciled this difference between binding masses. Including the support from residual gas motions in the hydrostatic cluster mass estimator improved the match with the true cluster mass (Rasia et al. 2004), with increasing kinetic pressure at larger cluster radii (Lau et al. 2009). The amount of energy in these bulk motions are of the order of 20% to 30% at radii of interest for cosmology (Battaglia et al. 2010; Burns et al. 2010). However, kinetic pressure support has only recently been included in analytical and semi-analytical templates for the thermal SZ power spectrum (Shaw et al. 2010; Trac et al. 2011). Of course cosmological hydrodynamical simulations fully include this contribution and thus do not require additional modeling of kinetic pressure effects. While of importance for correctly interpreting SZ measurements, the X-ray observations of clusters have been calibrated to partly take this effect into account when determining mass from the X-ray inferred total thermal energy (e.g., using the Y_X-M relation, Kravtsov et al. 2006).

In this paper, our focus is on the effects of bulk motions within clusters. These dominate the total kinetic pressure budget since there is generally a smaller fraction of energy in a hydrodynamical turbulent cascade compared to the energy on the injection scale which is well resolved for the relevant large scale motions. Quantifying turbulence in clusters is becoming feasible with simulations that include the modeling of sub-grid turbulence (e.g., Iapichino & Niemeyer 2008) as well as simulations with magnetohydrodynamics and anisotropic thermal conduction (Parrish et al. 2011).

The method of smoothed particle hydrodynamics (SPH) that we are using for solving the inviscid Euler equations in this work is perfectly suited for studying large-scale bulk motions which dominate the kinetic pressure support due to its Lagrangian and conservative nature. However, it is known that SPH in its standard implementation poorly resolves hydrodynamical instabilities, such as of Kelvin-Helmholtz or Rayleigh-Taylor type (Agertz et al. 2007). In non-radiative simulations of cluster formation, adaptively-refined mesh codes generate a larger core entropy level in comparison to SPH simulations which is presumably due to the difference in the amount of mixing in SPH and mesh codes and possibly related to a different treatment of vorticity in the simulations (e.g., Frenk et al. 1999; Mitchell et al. 2009; Vazza et al. 2011). A recent comparison of a galaxy formation simulation with the SPH technique and the recently developed moving mesh code AREPO

(Springel 2010) enabled – for the first time – to test the nature of the hydrodynamic solver with otherwise identical implementations of the gravity solver, the sub-resolution physics, and the detailed form of the initial conditions. The moving mesh calculations resulted in more disk-like galaxy morphologies in comparison to SPH. This difference originated from an artificially high heating rate with SPH in the outer parts of haloes, caused by viscous dissipation of inherent sonic velocity noise of neighboring SPH particles, an efficient damping of subsonic turbulence injected in the halo infall region potentially by the artificial viscosity employed by SPH, and because of a higher efficiency of gas stripping in AREPO (Vogelsberger et al. 2011). Based on these results it may be questionable to analyse small-scale velocity power spectra and 2-point structure functions in SPH simulations; however, the dominating large-scale bulk motions which is our primary interest should be followed accurately. This theoretical expectation is confirmed by analyzing otherwise identical cluster simulations run with AREPO and GADGET/SPH that show an equal kinetic pressure contribution outside the core region ($r > 0.05R_{200}$) for the two numerical techniques (Puchwein & Springel, priv. comm., 2011).

1.4. ICM shapes

DM halo shapes have been studied extensively. For SZ observations, the shape of the gas distribution of the ICM is important, especially in the far field of the intracluster medium which contributes substantially to the total integrated SZ flux (Battaglia et al. 2010). The assumption of spherical symmetry is often made when calculating cluster properties from observations and in analytical prescriptions so we would like to assess its validity. Semi-analytic models that employ the full three-dimensional information of a dissipationless dark-matter-only simulation use the shape of the resulting gravitational cluster potentials, so it is important to study how such shapes compare with those that include the dissipational gas component. Recent numerical work has shown the impact of cooling and star-formation on the properties of ICM shape for a sample size of 16 clusters (Lau et al. 2011), however, such a study has not been extended to a larger sample. Furthermore, the question of how energetic feedback in the cluster cores affects ICM shapes has not been addressed.

1.5. Overview

In this work we explore a large statistical sample of simulated clusters with identical initial conditions but employing different models for sub-grid physics. We quantify the importance of non-thermal pressure support and ICM shapes on the SZ Y-M scaling relation. In Section 2, we briefly describe the simulations and sub-grid physics used. We present our results for non-thermal pressure support from bulk motions and ICM shapes in Sections 3 and 4, respectively. The impact of these processes and changes in the simulated physics on the Y-M scaling relation is presented in Section 5. In Section 6 we summarize our results and conclude.

2. COSMOLOGICAL SIMULATIONS AND CLUSTER DATA SET

We described the basic suite of hydrodynamical models used in Battaglia et al. (2010). We simulate tens of large-scale boxes of the cosmic web in order to improve our statistics of the number of objects while simultaneously aiming for a sufficiently high mass resolution to map out the core regions of those clusters and groups which are the target of cur-

rent SZ cluster surveys and which dominate the SZ power spectrum signal on scales larger than 1'. Here we characterize the average behaviour of the properties of the ICM over a large mass and redshift range using a modified version of the GADGET-2 (Springel 2005) code which employs SPH and treePM for the gravity solver. For each modeled physics, we simulate a sequence of 10 boxes of side length $165\,h^{-1}\,\mathrm{Mpc} = 200\,\mathrm{Mpc}$ with periodic boundary conditions, encompassing $N_{\mathrm{DM}} = N_{\mathrm{gas}} = 256^3$ DM and gas particles. This gives an initial gas particle mass of $m_{\mathrm{gas}} = 3.2 \times 10^9\,h^{-1}\,\mathrm{M_\odot}$ and a DM particle mass of $m_{\mathrm{DM}} = 1.54 \times 10^{10}\,h^{-1}\,\mathrm{M_\odot}$. We adopt a minimum comoving (Plummer) gravitational smoothing length of $\varepsilon_{\mathrm{s}} = 20\,h^{-1}\,\mathrm{kpc}$. Our SPH densities are computed with 32 neighbours. For our standard calculations, we adopt a tilted ΛCDM cosmology, with total matter density (in units of the critical) $\Omega_{\mathrm{m}} = \Omega_{\mathrm{DM}} + \Omega_{\mathrm{b}} = 0.25$, baryon density $\Omega_{\mathrm{b}} = 0.043$, cosmological constant $\Omega_{\Lambda} = 0.75$, a present day Hubble constant of $H_0 = 100h\,\mathrm{km\,s^{-1}\,Mpc^{-1}}$ with $h = 0.7$, a spectral index of the primordial power-spectrum $n_{\mathrm{s}} = 0.96$ and $\sigma_8 = 0.8$.

We compare results for three variants of simulated physics: (1) the classic non-radiative 'adiabatic' case with only gravitational formation *shock heating*; (2) an extended *radiative cooling* case with star formation, supernova (SN) energy feedback and cosmic rays (CRs) from structure formation shocks (for more information on CRs, see Pfrommer et al. 2006a, 2007; Enßlin et al. 2007; Jubelgas et al. 2008); (3) *AGN feedback* in addition to radiative cooling, star formation, and SN feedback. Radiative cooling and heating were computed assuming an optically thin gas of primordial composition in a time-dependent, spatially uniform ultraviolet background. Star formation and supernovae feedback were modelled using the hybrid multiphase model for the interstellar medium of Springel & Hernquist (2003). The CR population is modelled as a relativistic population of protons described by an isotropic power-law distribution function in momentum space with a spectral index of $\alpha = 2.3$, following Enßlin et al. (2007). With those parameters, the CR pressure causes a small reduction in the integrated Compton-y parameter (Pfrommer et al. 2007), but can result in interesting modifications of the local intracluster y-map.

The AGN feedback prescription we adopt for our standard simulations (for more details see Battaglia et al. 2010) allows for lower resolution and hence can be applied to large-scale structure simulations. It couples the black hole accretion rate to the global star formation rate (SFR) of the cluster, as suggested by Thompson et al. (2005). If the SFR is larger than an observationally motivated threshold, $\dot{M}_* > 5\mathrm{M_\odot\,yr^{-1}}$, the thermal energy is injected into the ICM at a rate which is proportional to the SFR within a given spherical region. The AGN feedback in these box simulations injects approximately one third of total injected energy in the cluster formation phases at $z > 2$ (analogous to high-z QSO like feedback), another third in the redshift range $1 < z < 2$, and the final third below $z = 1$ (analogous to jet/bubble like feedback). These fractions depend moderately on the the numerical resolution; increasing the resolution enables to resolve the growth of smaller halos at earlier times and causes a higher fraction of energy injection at higher redshifts (see Battaglia et al. 2010, for a discussion).

We define the virial radius of a cluster, R_Δ, as the radius at which the mean interior density equals Δ times the *critical density*, $\rho_{\mathrm{cr}}(z)$ (e.g., for $\Delta = 200$ or 500). For comparison, we will use an alternative definition of the virial radius, $R_{\Delta,\mathrm{m}}$, where the mean interior density is compared to the *mean matter density*, $\bar{\rho}_{\mathrm{m}}(z)$. For clarity the critical density and the mean matter density are,

$$\rho_{\mathrm{cr}}(z) = \frac{3H_0^2}{8\pi G}\left[\Omega_{\mathrm{m}}(1+z)^3 + \Omega_\Lambda\right], \qquad (1)$$

$$\bar{\rho}_{\mathrm{m}}(z) = \frac{3H_0^2}{8\pi G}\Omega_{\mathrm{m}}(1+z)^3. \qquad (2)$$

Here we have assumed a flat universe ($\Omega_{\mathrm{m}} + \Omega_\Lambda = 1$) and are only interested in times after the matter-radiation equality, i.e., the radiation term with Ω_{r} is negligible. We chose to define the virial radius with respect to the critical density in continuity with recent cluster measurements. The merits and utilities of both these definitions are discussed later in Appendix C.

We apply the following two-step algorithm to compute the virial mass of a cluster in our simulations. First, we find all clusters in a given snapshot using a friends-of-friends (FOF) algorithm (Huchra & Geller 1982). Then, using a spherical overdensity method with the FOF values as starting estimates, we recursively calculate the center of mass, the virial radius, R_Δ, and mass, M_Δ, contained within R_Δ, and compute the radially averaged profiles of a given quantity with radii scaled by R_Δ. We then form a weighted average of these profiles for the entire sample of clusters at a given redshift unless stated otherwise. We use the integrated Compton y-parameter as our weighting function,

$$Y_\Delta = \frac{\sigma_{\mathrm{T}}}{m_{\mathrm{e}}c^2}\int_0^{R_\Delta} P_{\mathrm{e}}(r)4\pi r^2\,\mathrm{d}r \propto E_{\mathrm{th}}(< R_\Delta), \qquad (3)$$

where σ_{T} is the Thompson cross-section, m_{e} is the electron mass and P_{e} is electron pressure. For a fully ionized medium of primordial abundance, the thermal pressure $P = P_{\mathrm{e}}(5X_{\mathrm{H}}+3)/2(X_{\mathrm{H}}+1) = 1.932 P_{\mathrm{e}}$, where $X_{\mathrm{H}} = 0.76$ is the primordial hydrogen mass fraction.

3. NON-THERMAL CLUSTER PROFILES

Several simulations (Evrard 1990; Rasia et al. 2004; Lau et al. 2009) showed that the kinetic pressure from bulk motions contributes a small but still significant amount of energy within R_{500} and this importance increases for larger cluster radii (Lau et al. 2009; Battaglia et al. 2010; Burns et al. 2010). Thus, it is important to accurately quantify the kinetic pressure contribution as it biases the hydrostatic cluster masses and is significant to the total energy budget within clusters. There are two kinetic pressure contributions, namely large-scale, unvirialized bulk motions and subsonic turbulence. For a Kolmogorov power spectrum of turbulence, the energy is dominated by the largest scales which we resolved and characterize in our simulations. Hence we believe that our approach captures the majority of the kinetic pressure contribution.

3.1. Kinetic pressure support

The internal bulk motions in the medium can be quantified by the mass-averaged velocity fluctuation tensor, $\langle \delta V_i \delta V_j \rangle$, which is associate with the kinetic pressure (stress) tensor,

$$P_{\mathrm{kin},ij} = \rho\langle \delta V_i \delta V_j \rangle,$$
$$P_{\mathrm{kin}} \equiv \mathrm{Tr}\,\mathbf{P}_{\mathrm{kin}}/3 = \rho\langle \delta\mathbf{V}\cdot\delta\mathbf{V}\rangle/3,$$
$$\delta\mathbf{V} = a\,(\mathbf{v} - \bar{\mathbf{v}}) + aH(z)(\mathbf{x} - \bar{\mathbf{x}}). \qquad (4)$$

In this paper we focus on the trace, P_{kin}, which we refer to as the kinetic pressure. Issues associated with the anisotropic stress tensor will be made explicit where they appear, and are
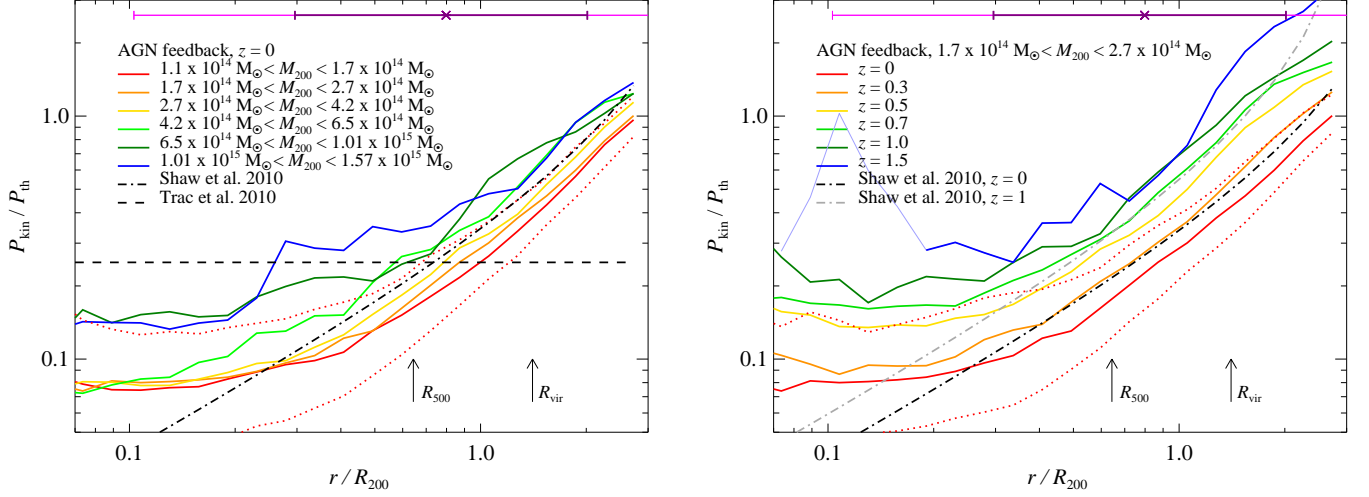
Figure 1. The ratio of kinetic and thermal pressure support, $P_{\rm kin}/P_{\rm th}$, depends on mass and redshift. We show the median of $P_{\rm kin}/P_{\rm th}$ as a function of radius for the AGN feedback simulations for various mass bins at $z = 0$ (left) and as a function of redshift for a fixed mass bin (right). We additionally show the $25^{\rm th}$ and $75^{\rm th}$ percentile values for the lowest mass bin at $z = 0$ (dotted). In both panels we illustrate the 1 and 2 σ contributions to Y_Δ centered on the median for the feedback simulation by horizontal purple and pink error bars which extends out to $4R_{200}$ (Battaglia et al. 2010). Two analytical models for the $P_{\rm kin}$ by Shaw et al. (2010) and Trac et al. (2011) are shown with the dash dot and dashed lines, respectively. The Shaw et al. (2010) model matches our result in the mass bin $2.7 \times 10^{14}\,{\rm M_\odot} \leq M_{200} \leq 4.2 \times 10^{14}\,{\rm M_\odot}$ at intermediate cluster radii (this mass bin best represents the mean mass of their sample at redshift zero), but also illustrates the need for a mass dependence in future analytical models. The dependence of $P_{\rm kin}/P_{\rm th}$ on cluster mass is driven by the variation of $P_{\rm kin}$ with mass (see Fig. 2 below).
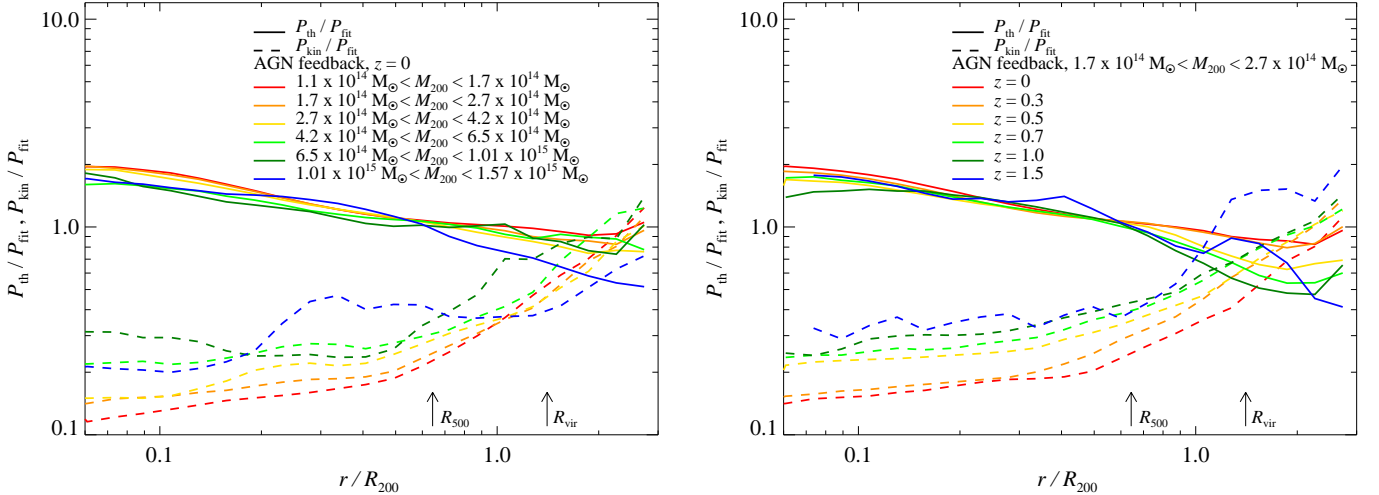

Figure 2. Mass and redshift dependence of $P_{\rm th}$ and $P_{\rm kin}$, normalized to an empirical fit from BBPS2, $P_{\rm fit}$, to the scaled thermal pressure, $P_{\rm th}/P_\Delta$. We show the mean scaled thermal and kinetic pressure profiles at $z = 0$ as a function of radius for the AGN feedback simulations in various mass bins (left), and for various redshifts at fixed mass bin (right).

also explored in more detail in BBPS3. The code uses comoving peculiar velocities, which are translated into the internal cluster velocities relative to the overall mean cluster velocity in the Hubble flow by the relation given, where $H(z)$ is the Hubble function, a is the scale factor, $\boldsymbol{v}$ ($= {\rm d}\boldsymbol{x}/{\rm d}t$) is the peculiar velocity and $\boldsymbol{x}$ is the comoving position of each particle. The gas-particle-averaged cluster bulk flow within R_{200} is $\bar{\boldsymbol{v}}$ and the center of mass within R_{200} is $\bar{\boldsymbol{x}}$.

The radial profiles of the kinetic-to-thermal pressure, $P_{\rm kin}/P_{\rm th}$, shown in Fig. 1 for various mass bins demonstrate an overall mass dependence at all cluster radii, predominately driven by the variation of $P_{\rm kin}$ and not $P_{\rm th}$ with mass. We show this explicitly in Fig. 2 where we scale $P_{\rm kin}$ with the virial ana-

logue of the thermal pressure,

$$P_\Delta \equiv GM_\Delta \Delta \rho_{\rm cr}(z) f_{\rm b}/(2R_\Delta), \ f_{\rm b} = \Omega_{\rm b}/\Omega_{\rm m}. \quad (5)$$

This behavior reflects the average formation history of galaxy groups and clusters which, according to the hierarchical picture of structure formation, sit atop the mass hierarchy, with the most massive clusters forming and virializing near to the present time. In contrast, the median galaxy group ($M_{200} = 10^{13}{\rm M_\odot}$) has stopped forming today as can be seen by the dramatically decreasing mass accretion rates implying that the associated virializing shocks have dissipated the energy associated with the growth of these objects and hence decreasing the kinetic pressure support (Wechsler et al. 2002; Zhao et al.

2009; Pfrommer et al. 2011). The semi-analytic model for non-thermal pressure support by Shaw et al. (2010) falls in the middle of the mass bins chosen since this model results from a sample of 16 high resolutions adaptive mesh refinement (AMR) simulations of individual galaxy clusters (Lau et al. 2009) which have a similar mass range. We provide a simple fit for the mass dependence of $P_{\mathrm{kin}}/P_{\mathrm{th}}$ in Appendix A. We find that the radius at which $P_{\mathrm{kin}} = P_{\mathrm{th}}$ is just beyond the spherical collapse definition for R_{vir} from Bryan & Norman (1998),

$$R_{\mathrm{vir}} = \left(\frac{3 M_{\mathrm{vir}}}{4\pi \, \Delta_{\mathrm{cr}}(z) \, \rho_{\mathrm{cr}}(z)} \right)^{1/3}, \qquad (6)$$

where $\Delta_{\mathrm{cr}}(z) = 18\pi^2 + 82[\Omega(z) - 1] - 39[\Omega(z) - 1]^2$ and $\Omega(z) = \Omega_{\mathrm{m}}(1+z)^3 \left[\Omega_{\mathrm{m}}(1+z)^3 + \Omega_\Lambda \right]^{-1}$. Hence, this radius represents a possible physical definition for the virialized boundary of clusters.

The redshift evolution of $P_{\mathrm{kin}}/P_{\mathrm{th}}$ is dramatic. At higher redshift, P_{kin} is increasing faster than P_{th} over all radii (cf. Fig. 2), such that at $z = 1$, $P_{\mathrm{kin}}/P_{\mathrm{th}}$ is approximately twice that at $z = 0$. In the picture of hierarchical structure formation, at any given redshift the most massive objects are currently assembled and hence show the largest kinetic pressure contribution in comparison to smaller objects that formed on average earlier. Or equivalently, at fixed cluster mass, the relative contribution from kinetic pressure and the relative amount of substructure increases with redshift. In particular, the relative mass accretion rates increase from $z = 0$ to $z = 2$ by a factor 3 for clusters ($M_{200} = 10^{15} \mathrm{M}_\odot$) and 10 for groups ($M_{200} = 10^{13} \mathrm{M}_\odot$) (see Pfrommer et al. 2011; Gottlöber et al. 2001). This strong evolution in $P_{\mathrm{kin}}/P_{\mathrm{th}}$ is lessened by a different choice of scaling radius, i.e., if we normalize by $R_{200,\mathrm{m}}$ instead of R_{200} (cf. Appendix C). Although this ratio cannot be observed, we will use it as an indicator for the dynamical state of clusters in our simulations. Results from Lau et al. (2009) find a similar correlation between P_{kin} and the X-ray definition of dynamical state, from a smaller sample of 16 clusters. At $z = 1$, the Shaw et al. (2010) semi-analytic model for non-thermal pressure support does not match our simulations as well as it does at redshift zero.[1]

The formation of clusters and the associated accretion of substructure are driven by the depth of the cluster gravitational potential. Therefore, it is not surprising that we find kinetic pressure support to be ubiquitous in the three differently simulated physics cases (cf. Fig. 3). Looking at the median of this non-thermal pressure support we find similar radial profiles within the 25th and 75th percentiles of the complete distribution of clusters. In the AGN feedback simulations we find marginally lower values for $P_{\mathrm{kin}}/P_{\mathrm{th}}$. These differences are well within the 25th and 75th percentiles implying consistency across differently modeled physics. Thus, our model of AGN feedback does not significantly alter the kinetic pressure support at low redshift although there seems to be a hint that this may be the case at larger radii at redshifts $z \sim 1$ which approach the peak of the AGN luminosity density.

We have so far focused on the trace of the kinetic pressure

---

[1] Our kinetic pressure contribution is larger at the center compared to that in the model by Shaw et al. (2010). This discrepancy is probably a manifestation of the well-known core entropy problem in numerical simulations. In (adaptive) grid codes there is a larger level of core entropy generated in comparison to SPH codes implying that the enhanced entropy (which results from dissipating gas motions) is accompanied by a smaller amount of kinetic pressure. This is presumably due to the difference in the amount of mixing in SPH and mesh codes and possibly related to a different treatment of vorticity in the simulations (e.g., Frenk et al. 1999; Mitchell et al. 2009; Vazza et al. 2011).
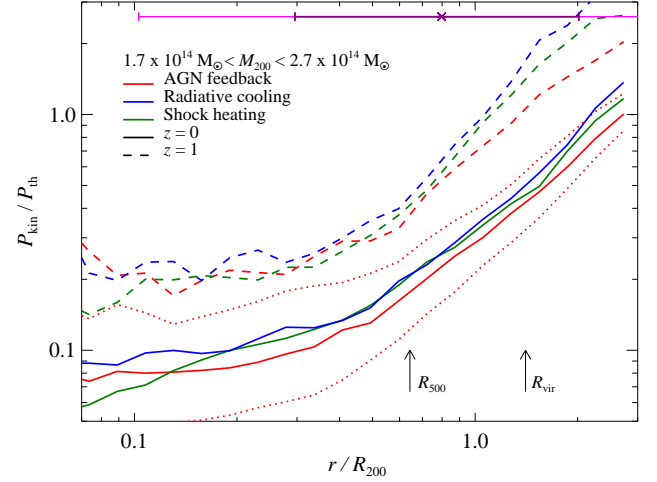

Figure 3. Shown is the median of $P_{\mathrm{kin}}/P_{\mathrm{th}}$ as a function of radius for different physics models at $z = 0$ (solid) and $z = 1$ (dashed) with the 25th and 75th percentile values shown for the AGN feedback simulations at $z = 0$ (dotted). Results are shown for the mass bin $1.7 \times 10^{14}\,\mathrm{M}_\odot \leq M_{200} \leq 2.7 \times 10^{14}\,\mathrm{M}_\odot$ to take out the dependence on mass of $P_{\mathrm{kin}}/P_{\mathrm{th}}$. The kinetic pressure contribution is similar for our differently simulated physics, suggesting that gravitational processes dictate that contribution (while AGN feedback slightly decreases the kinetic pressure contribution, especially for higher redshifts). The horizontal purple and pink error bars have the same meaning as in Fig. 1.
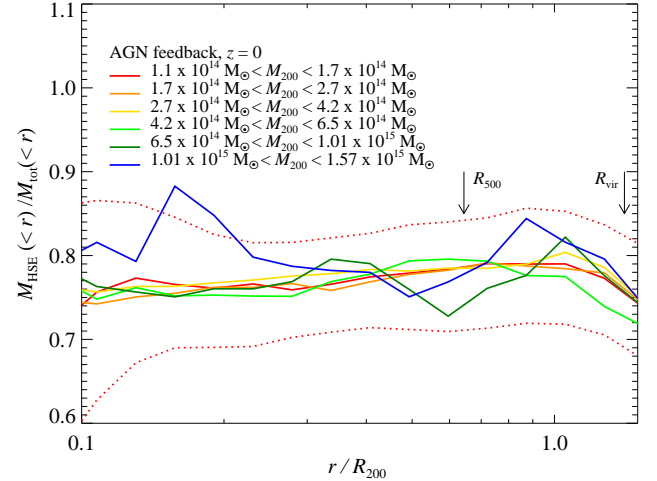

Figure 4. Assessing the bias in hydrostatic masses, M_{HSE}, due to the kinetic pressure. The median of $M_{\mathrm{HSE}}/M_{\mathrm{tot}}$ as a function of radius for AGN feedback simulations for various mass bins, with the 25th and 75th percentile values shown for the smallest mass bin (dotted). Assuming hydrostatic equilibrium for all clusters of a given mass will bias the mass values low by 20 to 25%. The scatter about the median – represented by the 25th and 75th percentiles – amounts to approximately 5%. This bias is not representative for a relaxed cluster sample which will likely have a smaller bias since the calibration of such a sample against numerical cluster simulations shows (Kravtsov et al. 2006).

tensor. We treat in detail the velocity anisotropy in BBPS3. The main results are that the core regions near the center, the velocity distribution starts to become isotropic for the gas in groups and (to a lesser extent) for the DM and gas in larger clusters. The positive values of velocity anisotropy around the virial radius indicate (radial) infall, whereas the strong decrease at even larger radii (very noticeably in the DM) is caused by the turn-around of earlier collapsed shells, which minimizes the radial velocity component such that the tangential components

dominate the velocity.

3.2. Hydrostatic Masses

Even if clusters are in hydrostatic equilibrium, balancing the gravitational force to the pressure gradient yields

$$\nabla P = \rho \boldsymbol{g} \rightarrow -\rho GM(<r)\hat{\boldsymbol{r}}/r^2 \text{ for spherical symmetry}, \quad (7)$$

and using this relation to estimate cluster masses will give the wrong result if one does not include non-thermal pressure, in particular the kinetic pressure.

As others have shown (Evrard 1990; Rasia et al. 2004; Lau et al. 2009), assuming that all the pressure in Eq. (7) is thermal ($P = P_{\rm th}$) is incorrect; for clarity we define $M_{\rm HSE}$ to be the mass derived using $P = P_{\rm th}$. Comparing $M_{\rm HSE}$ to the true mass inside a given radius, $M_{\rm tot}$, we find that $M_{\rm HSE}$ on average underestimates $M_{\rm tot}$ by 20–25% depending on the radius (cf. Fig 4). This bias is almost independent of cluster mass out to R_{500}, the current maximum radius typically observed by the X-ray telescopes *Chandra* and *XMM-Newton*. We can understand this weak mass dependence by rewriting the total pressure $P = P(P_{\rm th}/P + P_{\rm kin}/P)$. Since $P_{\rm kin}/P \propto M_{200}^{1/5}$ (see Fig. 19), the hydrostatic mass estimates inherit a similarly weak dependence on mass. Thus, an overall correction to the hydrostatic mass is reasonable for these measurements.

Individual clusters can stray from this generalization, since each cluster has a unique dynamical state and formation history. These deviations are suggested by the scatter of $\sim 5\%$ between the 25th and 75th percentiles of the complete distribution. For cluster samples that are selected against major mergers (for which the assumption of spherical symmetry will also be questionable), the correction factor will necessarily be smaller, e.g., for quality X-ray data of a Chandra sample, the hydrostatic mass correction was found to be of the order $M_{\rm HSE} \sim 10$–15% (Kravtsov et al. 2006).

4. CLUSTER SHAPES

Generally, we expect clusters to be triaxial since they grow by accretion and through merging along filamentary structures that impose tidal gravitational forces upon the forming clusters. Following Dubinski & Carlberg (1991), we estimate this non-sphericity of cluster gas and dark matter (DM) by computing the normalized moment-of-inertia tensor,

$$\langle \delta x \delta x \rangle_{ij}(r < R|w) = \frac{\sum_\alpha w_\alpha (x_{i,\alpha} - \bar{x}_i)(x_{j,\alpha} - \bar{x}_j)}{\sum_\alpha w_\alpha}, \quad (8)$$

for several weightings w_α of the contribution of particle α that lies within a given radius R. The tensor measures the variance in the spatial fluctuations within R, with $\delta x_i = x_i - \bar{x}_i$ the deviation of the particle position x_i from the centre-of-mass $\bar{x}_i(<R)$ of the region. Using mass weighting, $w_\alpha = m_\alpha$, for the dark matter or the SPH gas particles gives the moment-of-inertia in its usual form. It has an effective $\rho(x) x^5 d \ln x$ reach in its probe of the unit vector combination $\hat{\delta x}_i \hat{\delta x}_j$, hence preferentially feels the outskirts, near R. In the Appendix B, we explore how our results are modified with a weight $w_\alpha = m_\alpha/x_\alpha^2$ less sensitive to the outskirts: this weight just mass-averages the unit vector product, hence emphasizes the more isotropic interior. Since the tSZ signal is of primary interest to us, we also consider thermal-energy weighting, with $w_\alpha = m_\alpha T_\alpha$ the product of the mass and temperature.

We quantify the asphericity of cluster gas and DM by two parametrizations: the axis ratios (in particular the ratio of the largest-to-smallest main axis, c/a); and the three-dimensional asymmetry parameters for symmetric tensors introduced by BBKS (Bardeen et al. 1986). Both use the eigenvalues λ_i of the moment-of-inertia tensor at a prescribed radius, ordered by $\lambda_1 < \lambda_2 < \lambda_3$. The ellipsoid associated with the tensor has axis lengths $a = \sqrt{\lambda_1}$, $b = \sqrt{\lambda_2}$, and $c = \sqrt{\lambda_3}$. (We note that Lau et al. (2011) express their results in terms of eigenvalue ratios, defining $a' = \lambda_1$, $b' = \lambda_2$, and $c' = \lambda_3$). The eigenvectors $\boldsymbol{E}_i$ associated with λ_i are also used to rotate the clusters to their principal axes and to explore alignment variations with radius.

The BBKS-style asymmetry parameters are defined by

$$e = \frac{\lambda_1 - \lambda_3}{2\bar{\lambda}},$$
$$p = \frac{\lambda_1 - 2\lambda_2 + \lambda_3}{2\bar{\lambda}},$$
$$\bar{\lambda} \equiv \lambda_1 + \lambda_2 + \lambda_3. \quad (9)$$

Following BBKS (Bardeen et al. 1986), we refer to e as the ellipticity and p as the prolaticity. When p is positive the clusters are prolate, and when p is negative the clusters are oblate. Thus we also define the oblateness $o \equiv -p\theta(-p)$, equal to $|p|$ for negative p and zero for positive p. Although e is the most striking indicator of cluster elongation, the degree of prolateness or oblateness are also necessary to specify the general triaxiality of the morphological configuration on a given smoothing scale.

4.1. Overall shapes and their profiles

We rotate all clusters into the moment-of-inertia tensor frame using the eigenvector matrix $\boldsymbol{E}$, so $x' = \boldsymbol{E}x$. The output ordering is arbitrary; we choose the convention that the major axis is aligned with the x-axis and the minor axis is aligned with the z-axis. In Figs. 5 and 6 we show the results for DM and gas which have been obtained by computing the weighted moment-of-inertia tensor within $3R_{200}$, rotating into the moment-of-inertia tensor frame, and stacking the respective distributions, i.e., gas density and pressure as well as DM density. The rotated contours show obvious elongations along the major axis; with the ellipticity being larger at $z = 1$ in comparison to $z = 0$. The elongation is larger for the DM distribution in comparison to the gas density and pressure which show very similar behaviour. Even in the rotated stacked distributions, the innermost contour lines become more spherical because they are intrinsically less elliptical (see below) and because the main axes of the inner distributions are twisted relative to those at $3R_{200}$ so that their ellipticity partially averages out to become more spherical (see Sect. 4.5).

In order to quantify these results, we show the mass dependence and redshift evolution of the ellipticity within R_{200} in Fig. 7. Due to the dissipationless nature of DM, its ellipticity is larger (smaller ratio of c/a) in comparison to that of the gas. This is because the kinetic energy of the accreted gas is dissipated at cluster accretion shocks – a process that erases part of the memory of the geometry of the surrounding large scale structures and their tidal force field. Those accretion shocks are typically forming at radii $> R_{200}$ as suggested by numerical simulations (Miniati et al. 2000; Ryu et al. 2003; Pfrommer et al. 2006b; Skillman et al. 2008; Vazza et al. 2009) or indirectly by the action of shock waves on radio plasma bubbles, which represents a novel method of finding formation shocks (e.g., Ensslin et al. 2001; Pfrommer & Jones 2011). Following these qualitative considerations, it is not surprising that the ellipticity of the gas distribution does not show any mass dependence while the DM distribution of more massive
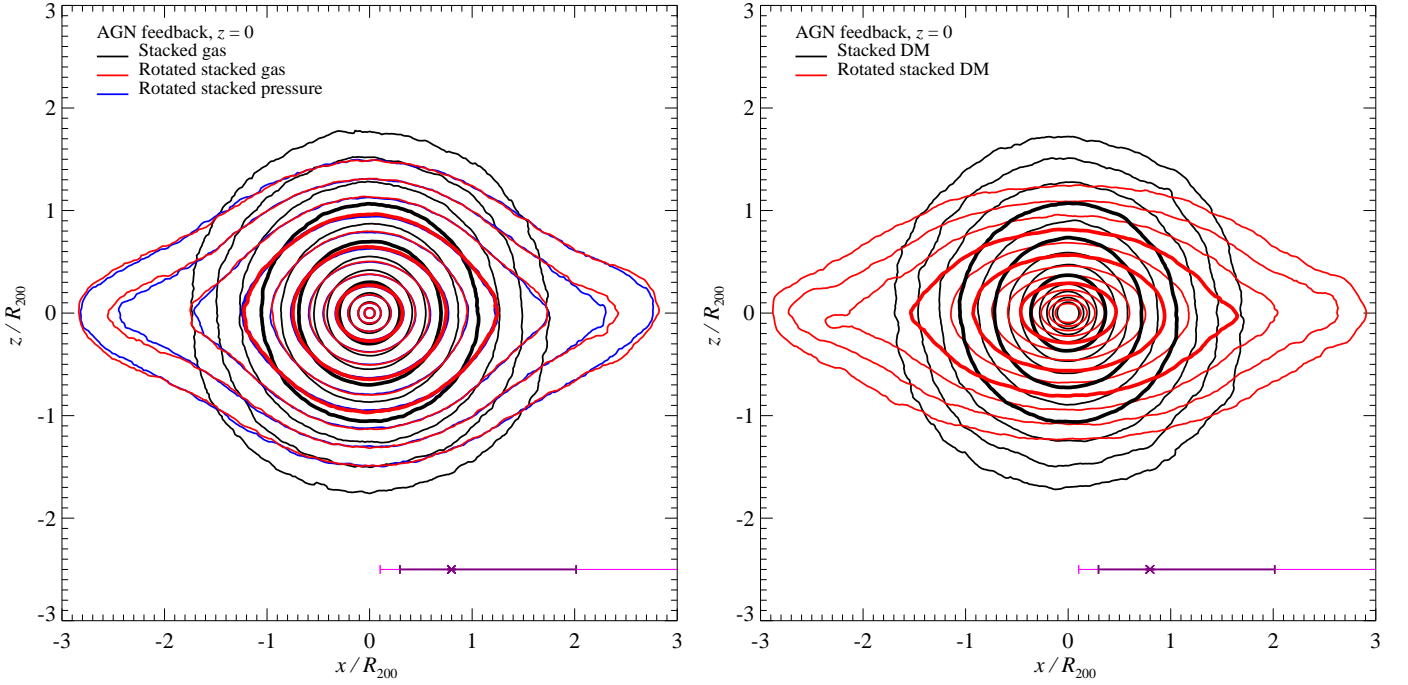
Figure 5. Stacked density and pressure distributions with and without rotations into the principle axis frame of the correspondingly weighted moment-of-inertia tensors at $z = 0$. Left: We compare rotated distributions of the gas density (red) and pressure (blue) to the non-rotated stacked gas density (black) at $z = 0$. Right: Shown is the same as on the left for DM. The non-rotated clusters average out to form spherical iso-density contours, while the rotated clusters clearly show elongations along the major axis (defined here as the x-axis). The thicker lines approximately show the radii R_{2500}, R_{500} and R_{200} from the inside out. These contours have been smoothed to a pixel size of $0.09R_{200}$. The horizontal purple and pink error bars have the same meaning as in Fig. 1.
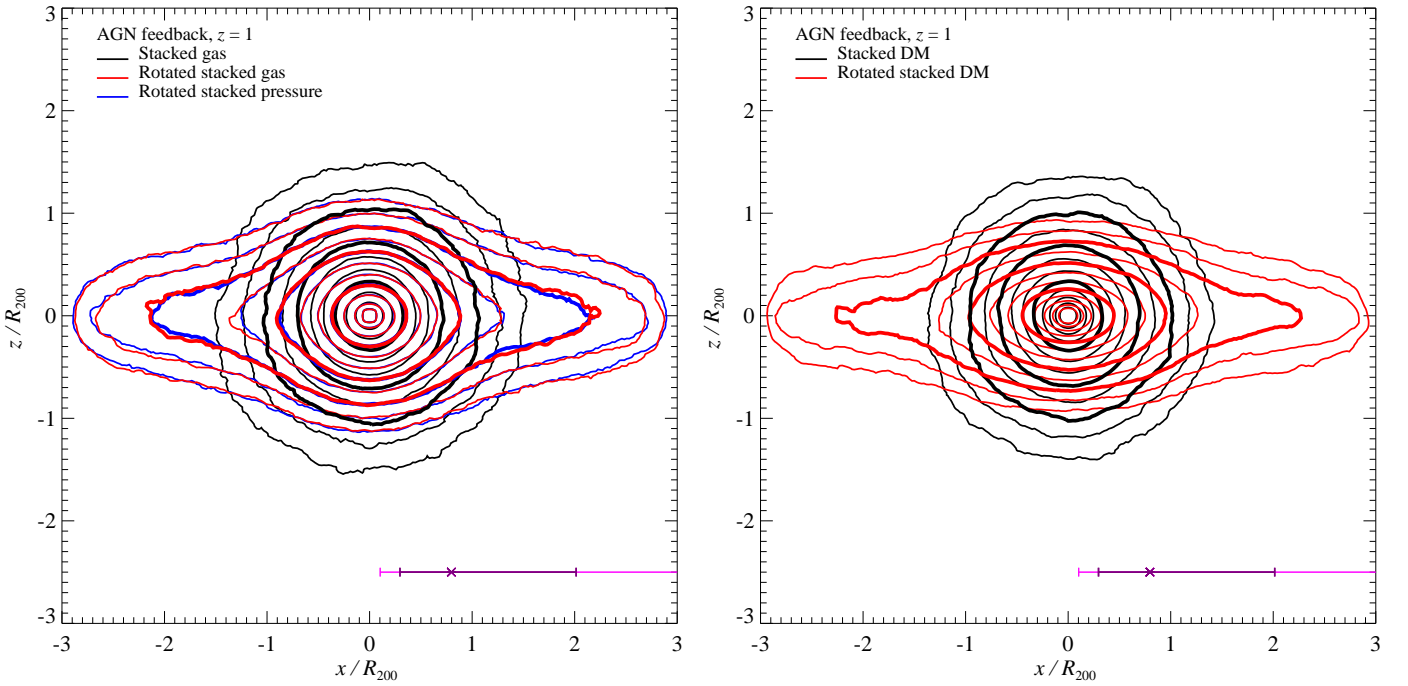
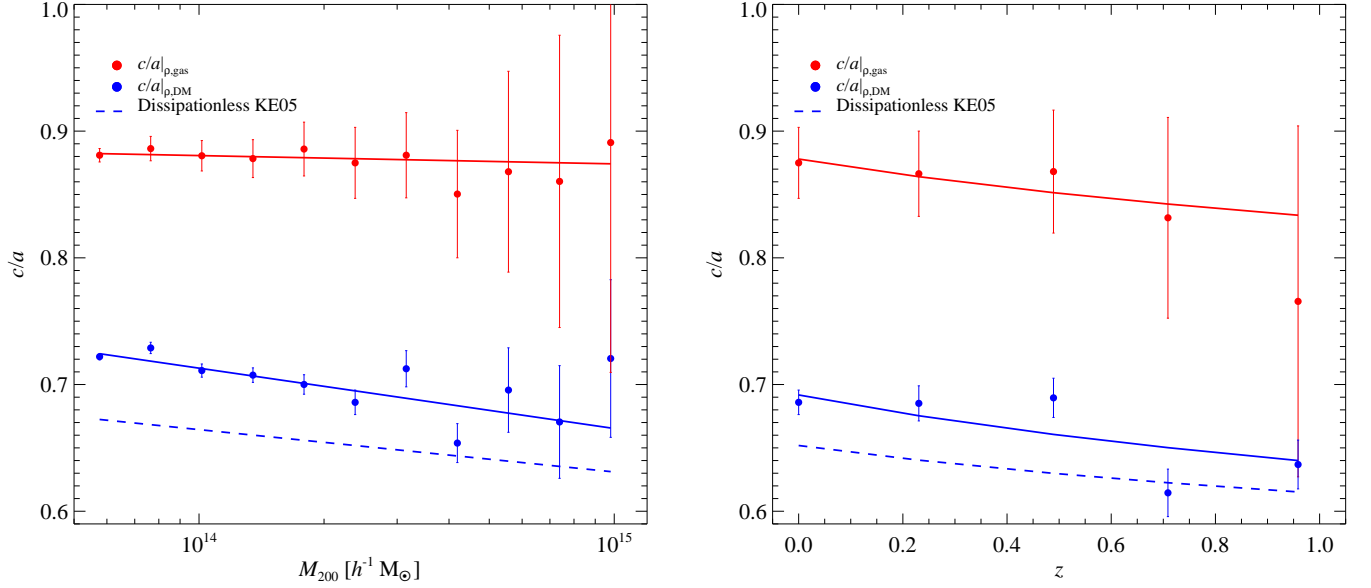**Figure 6.** Same as in Fig. 5, but at $z = 1$.

Figure 7. We show axis ratios of clusters that are obtained by computing the moment-of-inertia tensor of the gas (red) and DM mass distributions (blue) within R_{200} and stacking those in bins of cluster mass and redshift. The resulting mean and standard deviation of the axis ratio c/a is shown as a function of M_{200} at $z = 0$ (left panel) and at fixed average mass bin of $M_{200} = 2.4 \times 10^{14} h^{-1} M_{\odot}$ as a function z (right panel). See Table 1 for fit values; here, we have chosen to quote $h^{-1} M_{\odot}$ to compare directly with the dissipationless simulations by Kasun & Evrard (2005, KE05). Shocks dissipate the kinetic energy of the gas which causes larger axis ratios/smaller ellipticities, this couples through gravity to the DM distribution and sphericalize their axis ratios, resulting in smaller ellipticities in comparison to dissipationless simulations alone, e.g., by KE05 (that do not follow the hydrodynamics of the gas).
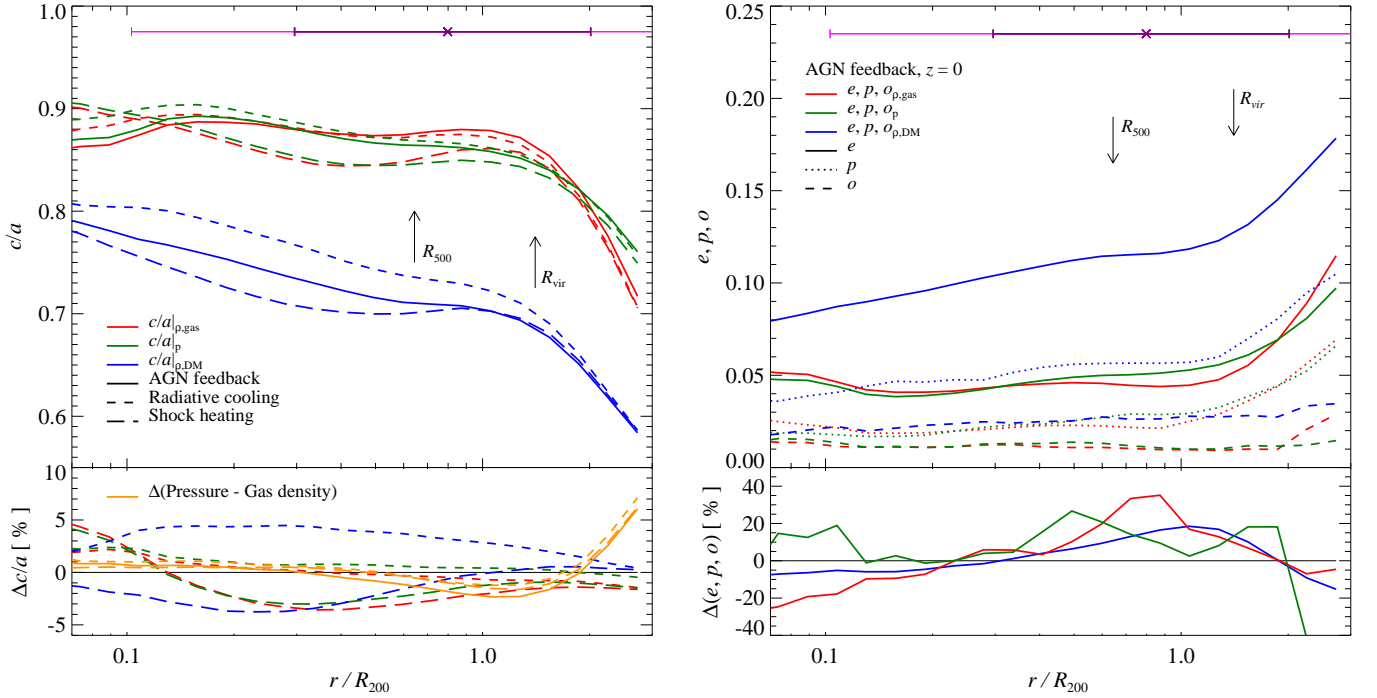

Figure 8. Average cluster axis ratios and ellipticities for the DM mass (blue), gas mass (red) and pressure (green) distributions within a scaled radius r/R_{200}. Left: Shown is the axis ratio c/a as a function of scaled radius for all simulated physics models. In the bottom panel we show the relative differences of the shock heating (long-dashed) and the radiative cooling simulations (short-dashed) with respect to AGN feedback simulations. Right: We show the ellipticity, prolaticity and oblaticity as a function of scaled radius. The bottom panel shows the relative differences between the pressure and gas density weightings of the moment-of-inertia tensor. The axis ratio c/a and ellipticity show the same trends. We find clusters to be more prolate then oblate. In the regions beyond $R_{\rm vir}$ the sudden decrease in the axis ratios can be attributed to other nearby groups and collapsed objects (that is also seen as an enhanced density clumping at these radii, Nagai & Lau 2011; Battaglia et al. 2011c). The pressure-weighted shapes tightly track the density-weighted shapes with deviations of less than 5%. The horizontal purple and pink error bars have the same meaning as in Fig. 1.

Table 1
Axis ratio fits for cluster as a function of mass and redshift.

	$B_{\rm M}$	$A_{\rm M}$	$B_{\rm z}$	$A_{\rm z}$
DM	0.665 ± 0.009	-0.031 ± 0.006	0.692 ± 0.009	-0.12 ± 0.04
KE05	0.631 ± 0.001	-0.023 ± 0.002	$0.652^a \pm 0.001$	-0.086 ± 0.004
Gas	0.87 ± 0.02	-0.003 ± 0.01	0.88 ± 0.03	-0.08 ± 0.12

^{a} We use a re-normalized value from $M_{200} = 1 \times 10^{15} h^{-1} M_\odot$
to $M_{200} = 2.4 \times 10^{14} h^{-1} M_\odot$.

clusters shows a larger ratio of c/a in comparison to smaller systems. However, the ellipticity of the gas and DM distribution are increasing as a function of redshift, at about the same rate. This can be understood by the fact that 1) a given mass range of clusters shows a larger degree of morphological disturbances/merging at higher redshifts which probe on average dynamically younger objects and 2) the redshift evolution of the velocity anisotropy (cf. BBPS3) which shows that the average location of accretion shocks moves to smaller radii (if scaled by R_{200}). Hence at larger redshifts, also the gas distribution probes the infall/pre-accretion shock region that is shaped by the tides exerted by the far-field of clusters.

We compare the results from our simulations directly with those of Kasun & Evrard (2005) in Figure 7 and Table 1. Other work (Allgood et al. 2006; Gottlöber & Yepes 2007; Macciò et al. 2008; Lau et al. 2011) on DM and gas shapes have used different mass definitions, axis definitions and cosmologies than we do, making quantitative comparisons difficult, but we note that these various results were shown to be consistent with Kasun & Evrard (2005). For the mass and redshift functional fits, Kasun & Evrard (2005) define $c/a(M) = B_{\rm M}(1 + A_{\rm M} \ln[M/10^{15} h^{-1} M_\odot])$ and $c/a(z) = B_{\rm z}(1+z)^{A_{\rm z}}$, respectively. The axis ratios that we find for the DM mass dependence and redshift evolution have slopes consistent with Kasun & Evrard (2005), but as an overall trend, our axis ratios are more spherical than theirs. Some of this may be traced to differing cosmological parameters, but some may be because the less aspherical baryons may have an impact on the DM ellipticity. The effect of baryons on DM has been explored in, e.g., Rudd et al. (2008).

In the following, we will show radial profiles of the axis ratios and asymmetric parameters that are obtained by computing the moment-of-inertia tensor at 30 different radii for each cluster. In Figure 8, we report on the overall radial distribution of c/a and ellipticity in the gas and DM distributions. Within R_{200}, the ellipticities of gas density and pressure are rather flat at a level of $c/a \simeq 0.85 - 0.9$. As laid out above, this is because dissipation effects at the accretion shocks cause an effective sphericalization and erase the memory of large-scale tidal fields. In contrast, ellipticities are increasing for the DM as a function of radius due to the dissipationless nature of DM, i.e. c/a decreases from values around 0.8 in the center to 0.7 at R_{200}. The radial behaviour may be due to increased tidal effects on DM substructures at small radii which causes a dramatic drop of their central mass density (Springel et al. 2008a,b; Pinzke et al. 2011). Effectively this causes a redistribution of a clumped (elliptical) to a smooth distribution that is able to couple more efficiently to the (more spherical) gas distribution. Studying the asymmetric parameters, we find that if a cluster is prolate, it is on average more elliptical than an oblate one that is always close to spherically symmetric.

We find that the average axis ratios and ellipticities have a
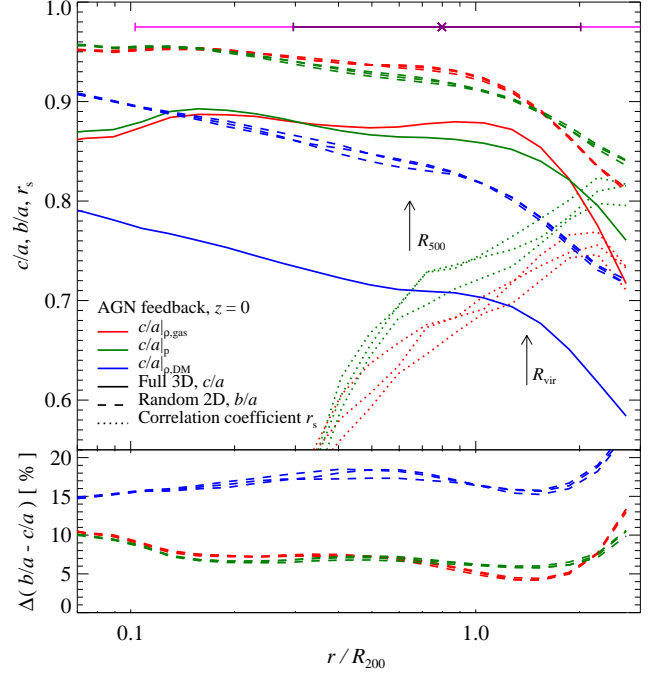

Figure 9. Top: We compare the average of the 2D axis ratios (dashed) of three random orthogonal projections to the 3D axis ratios (solid) for the DM mass (blue), gas mass (red) and pressure (green) from the clusters in the AGN feedback simulations. Additionally, we show the linear correlation coefficient, $r_{\rm s}$ (dotted line), between the projected 2D and the 3D axis ratios. The horizontal purple and pink error bars have the same meaning as in Fig. 1. Bottom: Shown is the relative differences between the projected 2D and 3D axis ratios. While the relative difference between the projected 2D and 3D axis ratios vary between 15–20% for the DM mass distribution (with the 2D axis ratios being more spherical), the relative differences are smaller for the mass and pressure distribution of the gas, with values between 5–10%. As expected, the projected 2D and the 3D axis ratios are correlated with an increasing correlation coefficient at larger radii which suggests that the substructure distribution that drives the asphericity also causes this correlation.

pronounced break in their slopes at $r \sim 1.5 R_{200}$. The break in the ellipticity arises from substructure in the cluster outskirts. Recent X-ray observations of the Perseus cluster find a strong signature of clumping in gas density (Simionescu et al. 2011); qualitatively consistent with the findings in simulations but not quantitatively (Nagai & Lau 2011). This gas density clumping is a direct tracer of substructure and becomes important at roughly the same radius where we find the break in the ellipticity. Interestingly, this effect is not only seen in DM and gas but also in pressure, which suggests that the pressure is clumped in a similar fashion as the gas density. In order to accurately model the outskirts of clusters, semi-analytic models will need to properly deal with the substructure. In the Appendix B, we show that one can attempt to counteract or lessen the impact of substructure on the gas, pressure and DM shapes by including an r^{-2}-weighting when calculating the moment-of-inertia tensor (cf. Eq. (8)). In future work, we will further explore the issue of substructure.

4.2. How shape profiles depend on modeled physics

We also address the influence that changes in the simulated physics has on cluster shapes in Fig. 8. While the ellipticity of the gas is slightly larger in non-radiative models, it is very similar for the gas distribution in our radiative models (radiative cooling and star formation with and without AGN feedback). Dissipating accretion shocks seem to explain the overall behavior rather well and the different physical models only

marginally change the cluster shapes in the gas. In the DM, however, there is still a pronounced difference among our two radiative physics models with the ellipticities of the AGN feedback model being larger that in our pure radiative model. This small ellipticity is a remnant of overcooling that our pure radiative model suffers with an associated star formation rate that is unphysically high. Most of these stars form out of the cold, dense gas in the core region which causes a decreasing central pressure support so that gas at larger radii moves in adiabatically and causes a deeper potential which in turn causes the DM to adiabatically contract. Enhanced dissipation processes in the gas sphericalize the potential which is then communicated to the DM during this central settling. We find that including AGN feedback counteracts the overcooling issue and modifies the DM shapes on the level of 5% in comparison to our pure radiative simulations (cf. Fig 8).

Our general trends are similar to those reported by Lau et al. (2011) who also find that the DM distribution is more spherical for radiative simulations in comparison to non-radiative models. However, the differences between radiative and non-radiative simulations are not as extreme as those found in Lau et al. (2011), since our radiative simulations do not have the level of (catastrophic) cooling in the central regions, because their simulations have higher resolution and include cooling from metals which we do not. The AGN feedback stabilizes the cooling and, thereby, lessens this sphericalizing effect on the DM ellipticity.

4.3. Projected and intrinsic shapes

In order to tie the underlying 3-dimensional structure of clusters to observable 2-dimensional projections, we compare the intrinsic 3D axis ratios to axis ratios of random 2D projections, i.e. we project the DM density and gas density/pressure distributions along a randomly chosen direction and then compute the 2D moment-of-inertia tensor. The results are shown in Figure 9. We find that the 2D axis ratios (b/a) for both, the gas density and pressure are systematically closer to unity than the 3D ratios c/a by $\sim$ 5–10% (for the virial region and the central part). In the case of the DM distribution, the projected (2D) axis ratios are on average a $\sim$ 15% underestimate of the intrinsic (3D) axis ratios. Using the linear correlation coefficient statistic (r_s), we find that the random 2D axis ratios are strongly correlated with the intrinsic 3D axis ratios with a radially increasing correlation strength (cf. Fig 9). As expected, c/a serves as a limit to the observable projected (2D) axis ratio. We find that the mean 2D axis ratio, as a function of cluster radius, closely tracks c/a, modulo a roughly constant $\sim 5-10\%$ bias (for the gas density and pressure).

4.4. Mass and redshift dependence of shape profiles

Both the density- and pressure-weighted ellipticities show the same general trends with radius and cluster mass. The ellipticity increases with increasing cluster mass by $\sim$ 50% over the mass ranges shown (cf. Fig 10). On the right-hand side of Fig. 10, we show the redshift evolution of the cluster shapes and find that the ellipticity is a stronger function of redshift than the mass. For increasing redshift, the break in the ellipticity profile moves to smaller radii (when scaled to R_{200}). Both behaviors, the mass and redshift dependence can be understood in the hierarchical picture for structure formation, where clusters show increased mass accretion rates and hence an increased level of substructure for larger clusters (at a given redshift) or, equivalently, for a cluster of given mass at higher redshifts which

probe on average systematically younger systems. Similar to the non-thermal pressure support, the redshift evolution found in the ellipticities are lessened by a different choice of scaling radius (cf. Appendix C). This result suggests that using a single (constant) ellipticity profile for clusters is not sufficient for percent level accuracy.

Pressure-weighted ellipticities are marginally more spherical than the density-weighted ellipticities for $r < R_{500}$ (cf. Figs. 8 and 10). However, between R_{500} and $2R_{500}$ the behavior is reversed. This is because the core region shows a smaller kinetic pressure support implying that hydrostatic forces had time to act and to smooth out the pressure distribution whereas at larger radii, pressure-weighted ellipticities are affected more by infall caused by a noticeable pressure clumping at these radii (cf. BBPS4). We have shown that scales around R_{500} are the most robust for studying the virial properties of clusters, since all ellipticities show only $\sim$ 10% redshift evolution and mass dependence on these scales. Taken together with the relatively modest degree of non-thermal pressure support on these scales found in § 3 and that these scales are far enough out to avoid the complications of the intricate "short-distance" physics of the cluster core region, we can give further justification for what is already the practice in the X-ray cluster community, driven by the nature of the X-ray data, namely a focus on R_{500} and environs for "global" cluster properties.

4.5. Alignment variations and semi-analytical models

Semi-analytic models for the baryon distribution in clusters include an underlying assumption that baryons will arrange themselves along equipotential surfaces (or in some cases the DM density-weighted surfaces). Given the importance of this assumption, we test its validity in our simulations. In Figure 7, we plot the ratio c/a for both dark matter and gas as function of cluster mass and redshift. While c/a for DM haloes decreases with halo mass as expected (Jing & Suto 2002), we find that c/a is constant for the gas distribution. This is potentially a problem for semi-analytic models of ICM gas (Ostriker et al. 2005; Bode et al. 2009), which solve for the resulting gas distribution in a DM-dominated gravitational potential as obtained from dissipationless simulations while allowing for a constant non-thermal pressure contribution (in the latter case). However, the gravitational potential from the DM is more spherical than the underlying matter distribution (e.g. Lau et al. 2011), and so the semi-analytic shape estimates are not as discrepant as one might expect from Figure 7.

A more important issue is the alignment of the gas or pressure with respect to the DM. We calculate the angular difference between the major axes of the DM and those of the gas and pressure major axes at a given radius, using the moment-of-inertia tensor eigenvectors $\boldsymbol{E}_{1,\mathrm{DM}}(r) \cdot \boldsymbol{E}_{1,\mathrm{gas}}(r)$. When calculating misalignment, the major axes of nearly spherical objects are poorly defined quantities. To avoid this problem we calculate, in each radial bin, a weighted average using $1 - c/a$ as the weight. Furthermore, we exclude the region inside $0.3R_{200}$ since the gas and pressure shapes are nearly spherical, with $c/a|_{\mathrm{DM}} > 0.75$. On average at a given radius, the cluster gas and pressure are $20-30$ degrees misaligned from the major axis of the DM (cf. Fig. 11). In the next section we show SZ measurements of the total thermal energy in clusters, Y, strongly depend on the projection axis through the cluster. Thus, misalignment between the semi-analytic baryon distortion and the "true" distribution may cause biases when using semi-analytic models to, *e.g.*, tie weak-lensing and SZ observations together.
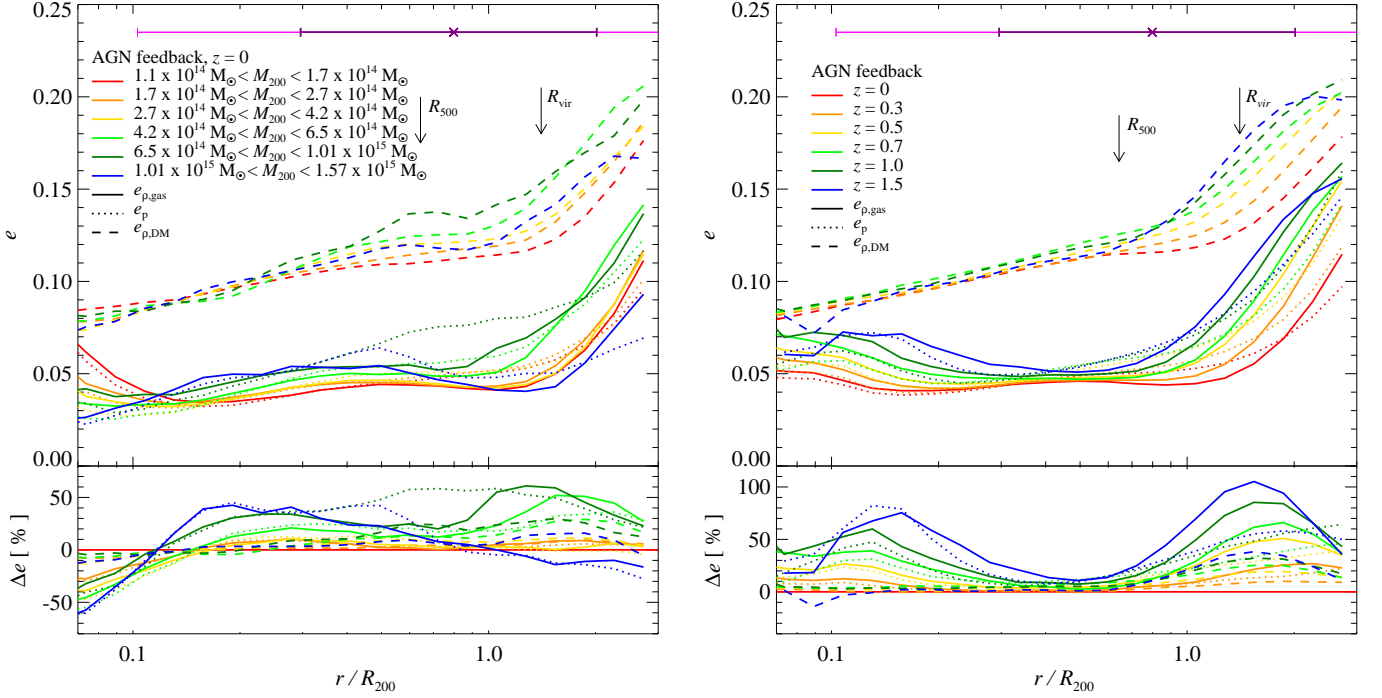
Figure 10. The dependence on mass and the redshift evolution of the cumulative ellipticity profile as a function of r/R_{200}. Left: Shown is the ellipticity profile at $z = 0$ for various mass bins. Bottom left: Shown are the relative differences in ellipticity to the lowest mass bin ($1.1 \times 10^{14}\,\mathrm{M_\odot} < M_{200} < 1.7 \times 10^{14}\,\mathrm{M_\odot}$). Over this mass range, the cluster ellipticities show a noticeable but not substantial mass dependence within R_{500}, in contrast to the stronger dependence on $P_{\mathrm{kin}}/P_{\mathrm{th}}$. Right: Shown is the ellipticity profile for various redshift bins. The horizontal purple and pink error bars have the same meaning as in Fig. 1. Bottom right: Shown is the relative difference of ellipticity at a given redshift to $z = 0$. The redshift evolution of the ellipticity (especially at large radii, $r > R_{500}$) is driven by the larger amount of substructures at higher redshifts due to the increased mass accretion rate of group/cluster halos at these redshifts. The pressure-weighted ellipticities track the density-weighted ellipticities well and show the same trends with redshift.
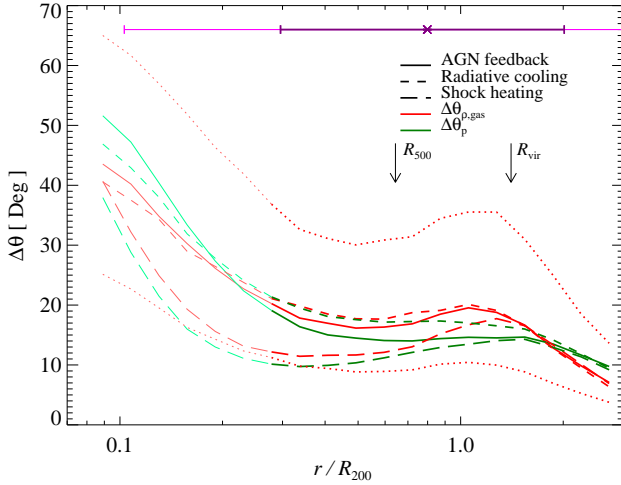

Figure 11. The weighted median angles between the DM major axis and gas (red) and pressure (green) axes at each radius for all simulated physics models: AGN feedback (solid), radiative cooling (short-dashed), and shock heating-only (long-dashed). The 25th and 75th percentile values are shown for the gas density in the AGN feedback model (dotted). On average the gas and pressure axes are misaligned by 20 to 30 degrees to the DM principle axis, independent of our simulated physics models. However, both simulations with radiative cooling show more misalignment in the inner regions than the non-radiative simulations. The light colors and lines represent the region where the average cluster shape is close to spherical ($c/a|_{\mathrm{DM}} > 0.75$) such that the major axes are not well defined and their angles are approaching a random distribution. Note that we have weighted the average angles by $1 - c/a$ to down-weight the angles from the spherical ICM shapes and the cluster interiors. The horizontal purple and pink error bars have the same meaning as in Fig. 1.

5. SZ SCALING RELATION

In this section we explore the impact of AGN feedback, cluster shapes and kinetic pressure support on the SZ-flux-to-mass relation, Y-M, using our large sample of clusters. We compute the SZ flux for all clusters for both, spherical boundaries and cylindrical apertures (Y_{sph} and Y_{cyl}). For the cylindrical aperture calculations the total fluxes are computed along each axis of the moment-of-inertia frame, measured at R_{200}, and additionally along each axis of another randomly-oriented frame. We choose the line of sight boundaries for the cylindrical integrations to be three times the radius of the aperture. This procedure enables quantifying the importance of substructure, which we have already shown in Sections 3 and 4 to be significant at radii beyond R_{200}. From the calculated Y_Δ values we fit an average scaling relation,

$$Y_\Delta = 10^B \left(\frac{M_\Delta}{3 \times 10^{14}\,h_{70}^{-1}\,M_\odot} \right)^A h_{70}^{-1}\,\mathrm{Mpc}^2, \qquad (10)$$

where A and B are the fit parameters for the slope and normalization, respectively. We weight each cluster by its Y_Δ when fitting for A and B to keep the low-mass clusters from completely dominating the fit.

5.1. Self-similar Y-M scaling relation

We review the expectations for Y in the idealized case of a cluster in virial equilibrium to help understand how possible deviations from the self-similar Y-M relation and the scatter about it may arise. Starting with Eq. (3), which has been
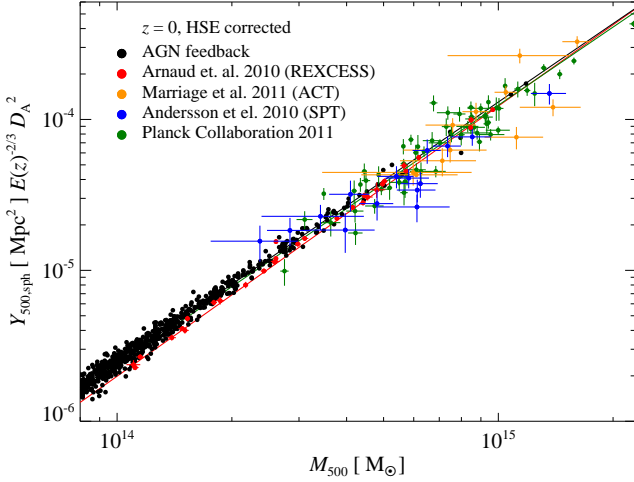
Figure 12. The Y-M scaling relation for the AGN feedback simulations compared to recent X-ray results from Arnaud et al. (2010) and SZ results from ACT (Marriage et al. 2010), SPT (Andersson et al. 2010), and *Planck* (Planck Collaboration et al. 2011a). We have applied the 15% correction to the X-ray M_{HSE} from Kravtsov et al. (2006).

rewritten as,

$$Y = \frac{\sigma_T}{m_e c^2} \int_0^{R_{200}} dV P_e = \frac{(\gamma - 1)\sigma_T}{m_e c^2} x_e X_H \mu E_{gas}, \quad (11)$$

where x_e is the electron fraction defined as the ratio of electron and hydrogen number densities $x_e = n_e/n_H = (X_H + 1)/(2X_H) = 1.158$, $\gamma = 5/3$ is the adiabatic index, $\mu = 4/(3X_H + 1 + 4X_H x_e) = 0.588$ denotes the mean molecular weight for a fully ionized medium of primordial abundance, and we assume equilibrium between the electron and ion temperatures. Next, we define the characteristic temperature of the halo (Komatsu & Seljak 2002) as

$$kT_{200} = \frac{GM_{200}\mu m_p}{3R_{200}} = \frac{\mu m_p}{3}[10 GH_0 M_{200} E(z)]^{2/3}, \quad (12)$$

so we can write the total thermal energy of the halo with Eq. (12) as

$$E_{gas} = \frac{3}{2} N_{gas} kT_{200} = (1 - f_*)f_b f_c \frac{GM_{200}^2}{2R_{200}}$$
$$= (1 - f_*)f_b f_c \frac{G}{2}[800 \rho_{cr}(z)]^{1/3} M_{200}^{5/3}. \quad (13)$$

Here $f_* \lesssim M_*/M_b$ is the stellar mass fraction within the halo and f_c is the correction factor for the fraction of missing baryons at a given overdensity. Then we insert Eq. (13) into Eq. (11) to get the integrated Compton-y parameter within R_{200},

$$Y = \frac{(\gamma - 1)\sigma_T}{m_e c^2} x_e X_H \mu(1 - f_*)f_b f_c G\left[\frac{\pi}{3}100\rho_{cr}(z)\right]^{1/3} M_{200}^{5/3}$$
$$= 97.6 h_{70}^{-1} \text{kpc}^2 E(z)^{2/3} \left(\frac{M_{200}}{10^{15} h_{70}^{-1}M_\odot}\right)^{5/3} \frac{\Omega_b}{0.043} \frac{0.25}{\Omega_m} \quad (14)$$

For Eq. (14), we set $f_* = 0$, $f_c = 0.93$ (as calculated from our shock heating simulations at R_{200}) and adopted the cosmological parameters of our simulation. This simple analytical expression for the Y-M scaling relation allows one to explore the assumptions underlying its derivation. More specifically, we test the assumptions of spherical gravitational potential, zero

non-thermal pressure support, and constant f_b (and for simulation with star formation, constant f_*) at R_Δ, independent of cluster mass.

5.2. Comparison to data

In Figure 12, we compare Y_{sph} for our simulated clusters to the X-ray results from Arnaud et al. (2010), and the SZ results from ACT (Marriage et al. 2010), SPT (Andersson et al. 2010), and *Planck* (Planck Collaboration et al. 2011a). We adopt the 15% correction to the X-ray M_{HSE} estimates from Kravtsov et al. (2006) which is valid for the respective observational sample selection criterion. Our Y_{sph}-M relation with AGN feedback is consistent with the current data from X-ray and SZ observations. However, at group scales, our simulations slightly overpredict the SZ flux due to the too high gas fractions, f_{gas}, in our simulations compared to X-ray observations (cf. BBPS4). Potentially our simulations are missing some of the relevant physics that governs f_{gas} (see, e.g., Pfrommer et al. 2011) or underestimate the action of AGN feedback on these mass scales.

The Y_{sph} reported by SZ surveys for known clusters use an X-ray-derived estimate of the aperture size. This is useful because the cluster radii are typically poorly measured in SZ, and so the X-ray aperture fixes the SZ measurement along the otherwise degenerate aperture flux/aperture radius relation. However, this prior introduces correlations between the X-ray and SZ observations, which makes comparisons between these observations difficult to interpret.

5.3. Physics dependence of the Y-M relation

In Figure 13 we show the dependence of the Y-M relation on our three simulated physics models, i.e., shock heating, radiative cooling and star formation, and AGN feedback. The stark differences between the shock heating simulation and the two radiative simulation models arise from the loss of baryons in the ICM to star formation. The radiative cooling simulations show a constant normalization offset of $\sim 20\%$, which nearly matches the f_* values for these simulations. In Table 2 we show that the self-similar expectation of Eq. (14) almost completely captures the cluster thermodynamics in our simulations when integrated over cluster-sized apertures. Including more physically motivated sub-grid models in the simulations, we find that both, the shock heating and radiative cooling slopes are consistent with this self-similar derivation for the Y-M relation, while the AGN feedback simulations have a steeper, mass-dependent slope. This break from self-similarity in the AGN simulations arises from the suppression of star formation in the higher mass clusters and a feedback-induced deficit of gas inside the lower mass clusters. Over the redshift ranges we explore ($z = 0$ to $z = 1.5$) and for all simulated physics models, the Y-M scaling relation normalization changes as predicted by self-similar evolution and the slopes remain essentially constant (cf. Fig. 14). So, the Y-M relations from AGN simulations are different at $z = 0$, but evolve as predicted by self-similar evolution. This result is independent of the two aperture sizes chosen, which correspond to over-densities of 200 and 500 times the critical density (Fig. 14). As we have repeatedly found in previous sections, the clusters interior to the radii R_{500} and even R_{200} are relatively well behaved, with only modest impact of cluster ellipticities and kinetic pressure.

To quantify the scatter, we compute the relative deviation of each cluster from the mean relation, $\delta Y_\Delta/Y = (Y_\Delta - Y_{\Delta,\text{fit}})/Y_{\Delta,\text{fit}}$, and then fit this distribution with a Gaussian prob-

Table 2
Y-M scaling relation fits for different simulated physics, sub-sampling in kinetic-to-thermal energy and ellipticity (of the density and pressure distribution), and along different projected axes yielding Y_{cyl}.

$\Delta = 200$	$z = 0$			$z = 0.5$			$z = 1$		
	B	A	σ_Y	B	A	σ_Y	B	A	σ_Y
Simulated physics									
Theory, Eq. (14)	-4.88	1.67	-	-4.81	1.67	-	-4.74	1.67	-
Shock heating	-4.87 ± 0.01	1.64 ± 0.03	0.115 ± 0.001	-4.81 ± 0.02	1.63 ± 0.04	0.116 ± 0.001	-4.76 ± 0.05	1.61 ± 0.07	0.111 ± 0.002
Radiative cooling	-4.94 ± 0.01	1.67 ± 0.03	0.119 ± 0.001	-4.88 ± 0.02	1.67 ± 0.05	0.121 ± 0.002	-4.83 ± 0.05	1.66 ± 0.09	0.121 ± 0.002
AGN feedback	-4.92 ± 0.01	1.71 ± 0.03	0.133 ± 0.001	-4.87 ± 0.02	1.72 ± 0.05	0.136 ± 0.002	-4.82 ± 0.05	1.73 ± 0.09	0.147 ± 0.003
K/U^a									
Lower 3rd	-4.88 ± 0.04	1.73 ± 0.07	0.115 ± 0.002	-4.83 ± 0.06	1.73 ± 0.11	0.122 ± 0.003	-4.78 ± 0.14	1.76 ± 0.21	0.137 ± 0.004
Middle 3rd	-4.92 ± 0.02	1.73 ± 0.05	0.116 ± 0.002	-4.87 ± 0.04	1.73 ± 0.08	0.121 ± 0.003	-4.82 ± 0.07	1.73 ± 0.13	0.138 ± 0.005
Upper 3rd	-4.94 ± 0.02	1.72 ± 0.04	0.123 ± 0.002	-4.89 ± 0.03	1.73 ± 0.07	0.122 ± 0.003	-4.85 ± 0.09	1.72 ± 0.15	0.141 ± 0.005
c/a (gas)^a									
Lower 3rd	-4.94 ± 0.02	1.72 ± 0.05	0.131 ± 0.002	-4.89 ± 0.04	1.72 ± 0.08	0.133 ± 0.003	-4.84 ± 0.09	1.73 ± 0.15	0.147 ± 0.005
Middle 3rd	-4.92 ± 0.02	1.70 ± 0.05	0.129 ± 0.002	-4.86 ± 0.05	1.73 ± 0.09	0.133 ± 0.003	-4.82 ± 0.10	1.72 ± 0.16	0.136 ± 0.004
Upper 3rd	-4.90 ± 0.02	1.72 ± 0.05	0.119 ± 0.002	-4.86 ± 0.04	1.72 ± 0.08	0.123 ± 0.003	-4.80 ± 0.09	1.73 ± 0.15	0.138 ± 0.004
c/a (pressure)^a									
Lower 3rd	-4.94 ± 0.02	1.71 ± 0.05	0.132 ± 0.002	-4.88 ± 0.04	1.73 ± 0.08	0.134 ± 0.003	-4.84 ± 0.08	1.73 ± 0.14	0.152 ± 0.005
Middle 3rd	-4.92 ± 0.03	1.71 ± 0.05	0.129 ± 0.002	-4.87 ± 0.04	1.72 ± 0.08	0.128 ± 0.003	-4.82 ± 0.08	1.72 ± 0.14	0.134 ± 0.004
Upper 3rd	-4.90 ± 0.03	1.72 ± 0.05	0.122 ± 0.002	-4.86 ± 0.05	1.71 ± 0.09	0.129 ± 0.003	-4.78 ± 0.12	1.76 ± 0.19	0.137 ± 0.004
b/a (gas)^a									
Lower 3rd	-4.93 ± 0.02	1.70 ± 0.04	0.138 ± 0.007	-4.88 ± 0.04	1.72 ± 0.07	0.140 ± 0.010	-4.83 ± 0.07	1.73 ± 0.12	0.149 ± 0.016
Middle 3rd	-4.92 ± 0.02	1.71 ± 0.05	0.130 ± 0.006	-4.87 ± 0.04	1.72 ± 0.08	0.137 ± 0.009	-4.83 ± 0.11	1.72 ± 0.18	0.149 ± 0.014
Upper 3rd	-4.91 ± 0.02	1.72 ± 0.05	0.128 ± 0.002	-4.86 ± 0.04	1.72 ± 0.07	0.132 ± 0.003	-4.81 ± 0.09	1.73 ± 0.14	0.136 ± 0.004
Y_{cyl} rotated^a									
Minor axis	-4.87 ± 0.01	1.69 ± 0.03	0.126 ± 0.001	-4.83 ± 0.02	1.69 ± 0.05	0.136 ± 0.002	-4.79 ± 0.05	1.70 ± 0.09	0.144 ± 0.003
Middle axis	-4.87 ± 0.01	1.69 ± 0.03	0.128 ± 0.001	-4.82 ± 0.02	1.69 ± 0.05	0.133 ± 0.002	-4.78 ± 0.05	1.69 ± 0.09	0.147 ± 0.003
Major axis	-4.84 ± 0.01	1.68 ± 0.03	0.137 ± 0.002	-4.79 ± 0.02	1.67 ± 0.05	0.152 ± 0.002	-4.74 ± 0.05	1.68 ± 0.09	0.167 ± 0.003
Y_{cyl} random^a									
axis 1	-4.86 ± 0.01	1.69 ± 0.03	0.129 ± 0.001	-4.82 ± 0.02	1.69 ± 0.05	0.140 ± 0.002	-4.77 ± 0.05	1.70 ± 0.09	0.146 ± 0.003
axis 2	-4.86 ± 0.01	1.69 ± 0.03	0.129 ± 0.001	-4.82 ± 0.02	1.69 ± 0.05	0.138 ± 0.002	-4.78 ± 0.05	1.68 ± 0.09	0.150 ± 0.003
axis 3	-4.86 ± 0.01	1.69 ± 0.03	0.130 ± 0.001	-4.82 ± 0.02	1.69 ± 0.05	0.141 ± 0.002	-4.77 ± 0.05	1.70 ± 0.09	0.152 ± 0.003

^{a} For fits to all sub-samples/projections, we use our AGN feedback model. Fit parameters are defined in Eq. (10).
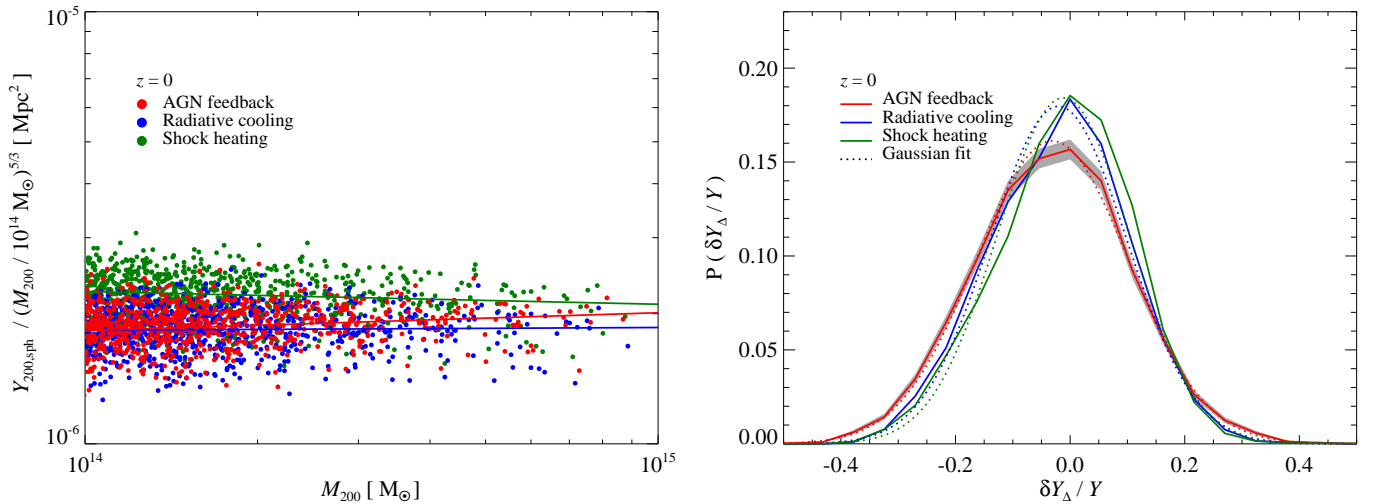^{b} For the b/a sub-sampling of Y_{cyl}, we chose random axis 1.

Figure 13. The normalization, slope and scatter of the Y-M scaling relations all depend on the simulated physics. Left: The Y-M scaling relations at $z = 0$ for all simulated physics models: shock heating (green), radiative cooling (blue), and AGN feedback (red). The y-axis has been scaled by $M^{5/3}$ to highlight the deviations from self-similarity. Right: The probability distributions for the relative deviation, $\delta Y_\Delta/Y$, with respect to the best fits for all three physics models. We also show Gaussian fits (dotted lines) and include Poisson deviations for the AGN feedback simulations (grey band). We find that the AGN feedback simulations have the largest scatter and a steeper slope compared to the other simulations.
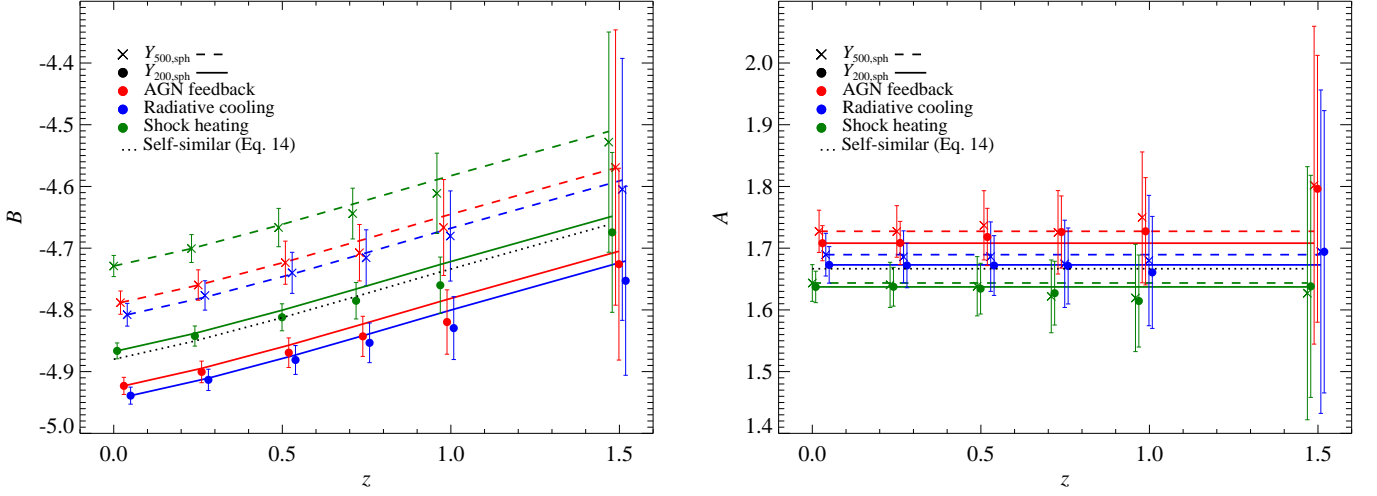
Figure 14. All simulated Y-M scaling relations evolve self-similarly with redshift according to Eq. (14). We show the Y-M scaling relation fits for the normalization, B, (left panel) and slope, A, (right panel) as a function of redshift and for two different cluster masses M_{200} and M_{500}, and compare those to the self similar prediction for M_{200} (dotted black). The Y-M relation of AGN feedback simulations has a different slope, but shows no anomalous redshift evolution relative to self-similar evolution.
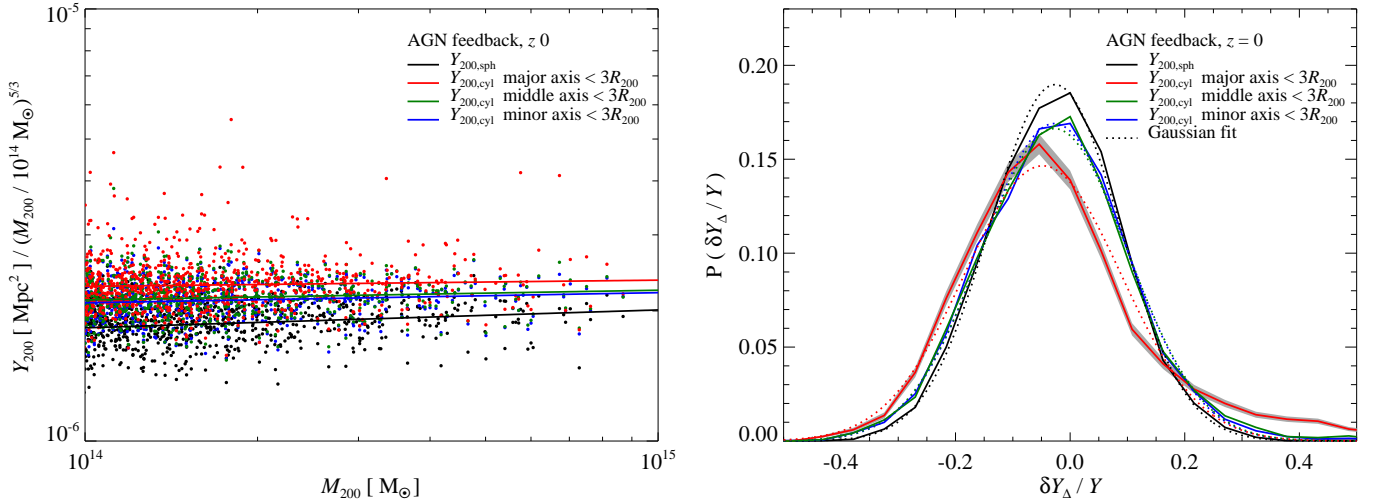
Figure 15. Rotating the clusters into their major, middle and minor axes and calculating projected (cylindrical) Y-M relations shows the effect of infalling substructure. Left: The cylindrical Y-M scaling relations from the AGN simulations for clusters that have been rotated into their major, middle, and minor axes defined by computing the (3D) moment-of-inertia tensor within R_{200}. Right: The probability distributions for the scatter, δY_Δ, relative to the best fits for all three distributions, each representing a distinctive rotation as well as the spherical distribution (black). We include the Gaussian fits (dotted lines) and the Poisson deviations for the major axis rotation (grey band). Rotating the clusters such that integration happens along the major axis increases the total Y values, while further distorting and increasing the scatter (due to the large cluster-to-cluster variance in the infall regions). The $Y_{\rm cyl}$ values are integrated along the given axis from $-3R_{200}$ to $3R_{200}$; hence for any given cluster $Y_{\rm cyl} \geq Y_{\rm sph}$.
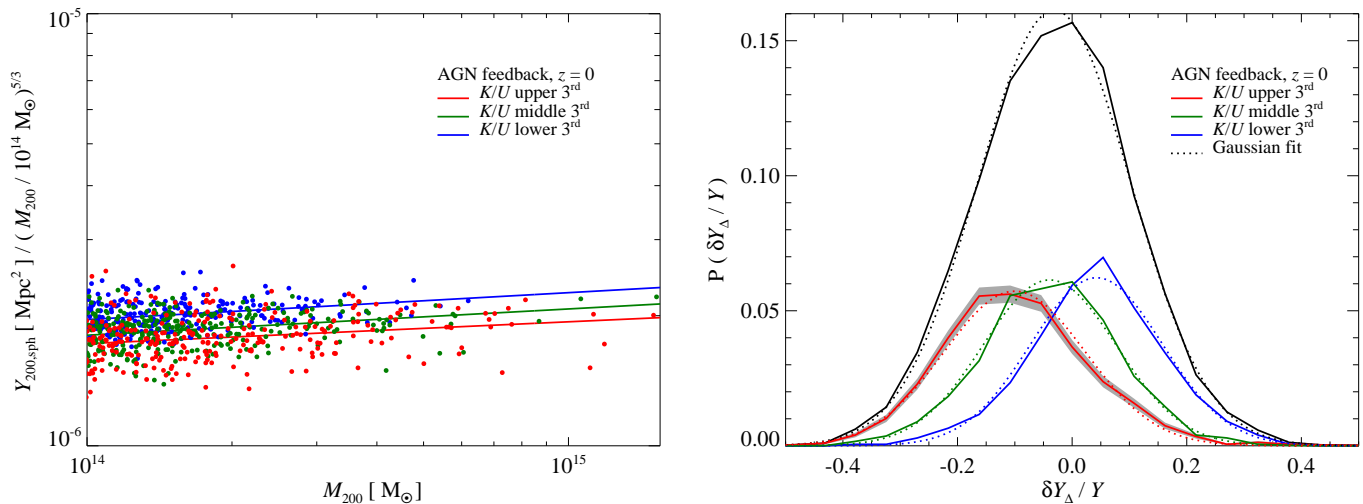
Figure 16. Sub-sampling the Y-M relations by the kinetic-to-thermal energy ratio (K/U) for the AGN simulations. Left: The Y-M scaling relation for the three K/U sub-samples, upper 3rd (red), middle 3rd (green) and lower 3rd (blue), with the corresponding slope fitted to those points. The y-axis has been scaled by $M^{5/3}$ to highlight the deviations from self-similarity. Right: The probability distributions for the relative deviation, $\delta Y_\Delta/Y$, with respect to the best fits for the three sub-samples and the total distribution (black), including the Gaussian fits (dotted lines) and the Poisson deviations for the upper 3rd sub-sample (grey band). The sub-sample of K/U with the largest kinetic pressure support (upper 3rd) shows systematically lower total Y values for a given mass as well as larger scatter, while the lower K/U sub-sample has the lowest scatter of $\sim 11\%$. This is expected because a larger kinetic pressure contribution implies a lower thermal pressure and hence decreases Y.

ability distribution function (PDF),

$$G(\delta Y_\Delta/Y) = A_0 \exp\left[\frac{-(\delta Y_\Delta/Y)^2}{2\sigma_Y^2}\right]. \qquad (15)$$

Here the parameter A_0 is the normalization and σ_Y is the variance, which we will refer to as the scatter. Here we have chosen to model the variation about the mean as a Gaussian, while previous work by Stanek et al. (2010) showed that a log-normal distribution is also a reasonable description of the scatter. In Appendix D, we show that within the (Poisson) uncertainties, the scatter is clearly Gaussian distributed and only approximately log-normal. Forcing a log-normal distribution introduces higher-order moments such as skewness and kurtosis as can be seen by the tails in the distributions and their asymmetric shapes.

We find that the scatter, σ_Y, for the entire sample of clusters is between 11 % and 13 % (cf. Fig. 13 and Table 2), which is consistent with previous work (Nagai 2006; Shaw et al. 2008; Stanek et al. 2010; Yang et al. 2010). In the simplest simulations with only shock heating the source for this scatter in the Y-M relation has been proposed to arise from the formation time, the concentration, and the dynamical state of the cluster (Yang et al. 2010). As our simulations include more sub-grid physics models the scatter increase from $\sim 11\%$ to $\sim 13\%$ at $z = 0$ and changes further from $\sim 11\%$ to $\sim 15\%$ at $z = 1$. Of the three different physics models, the simulations with AGN feedback gives the largest scatter, which is consistent with semi-analytic results (Shaw et al. 2008). This model for AGN feedback is self-regulated (Battaglia et al. 2010) and injects $\sim 2/3$ of the energy before $z = 1$ when the average cluster mass is significantly smaller and the associated potentials are shallower so that a fixed energy injection by AGNs may in principle have a stronger impact[2]. Thus, the increased scatter in the Y-M relation from the AGN feedback simulations compared to the sim-

ulations without feedback is a result of the energy injection, which heats and disturbs the ICM. This statement is in accordance with previous results from Battaglia et al. (2010), where they showed the impact of AGN feedback on the pressure profiles of clusters and found that simulations with feedback had a shallower asymptotic pressure profile slopes than those without feedback. Thus, the intermittent nature of energy injection into the group system early-on results in a larger scatter in the Y-M relation compared to simulations without energetic feedback.

5.4. Cylindrical Apertures

For pointed SZ observations of clusters and SZ surveys, a natural, model-independent observable is the projected flux, Y_{cyl} (Mroczkowski et al. 2009; Sayers et al. 2011). We find $Y_{cyl} > Y_{sph}$ in all cases, whether we chose the projection along a principal or a random axis. This is due to the assumed extension along the line-of-sight integration which we choose to be three times the aperture radius; in observations, structure beyond this scale may additionally contribute in some cases. In fact, a projection integral out to $3R_{200}$ decreases the Y-M slope for the AGN feedback simulations such that it becomes consistent with the self-similar slope (cf. Table 2). We find no difference between the random 2D projections and the integration along the middle or minor axes with respect to the normalization and slope (cf. Fig. 15 and Table 2). The scatter for the random 2D projections is marginally larger than the projections along middle and minor axes. Our results show that the integration along the major axis yields dramatically different results, both, for the normalization and scatter in comparison to projections along the other axes. This has its origin in the more extended tails of the PDF (cf. Fig 15). The normalization and scatter between the major axis and the other axes increase by $\sim 7\%$ and $\sim 9\%$, respectively. At a higher redshifts, these differences are amplified and we find a $\sim 12\%$ increase in the normalization and an increase in scatter by $\sim 16\%$. This indicates that substructure is preferentially aligned with major axis and that substructure heavily influences the result from the

---

[2] Similar results were found by McCarthy et al. (2011) in simulations with a more detailed feedback prescription.
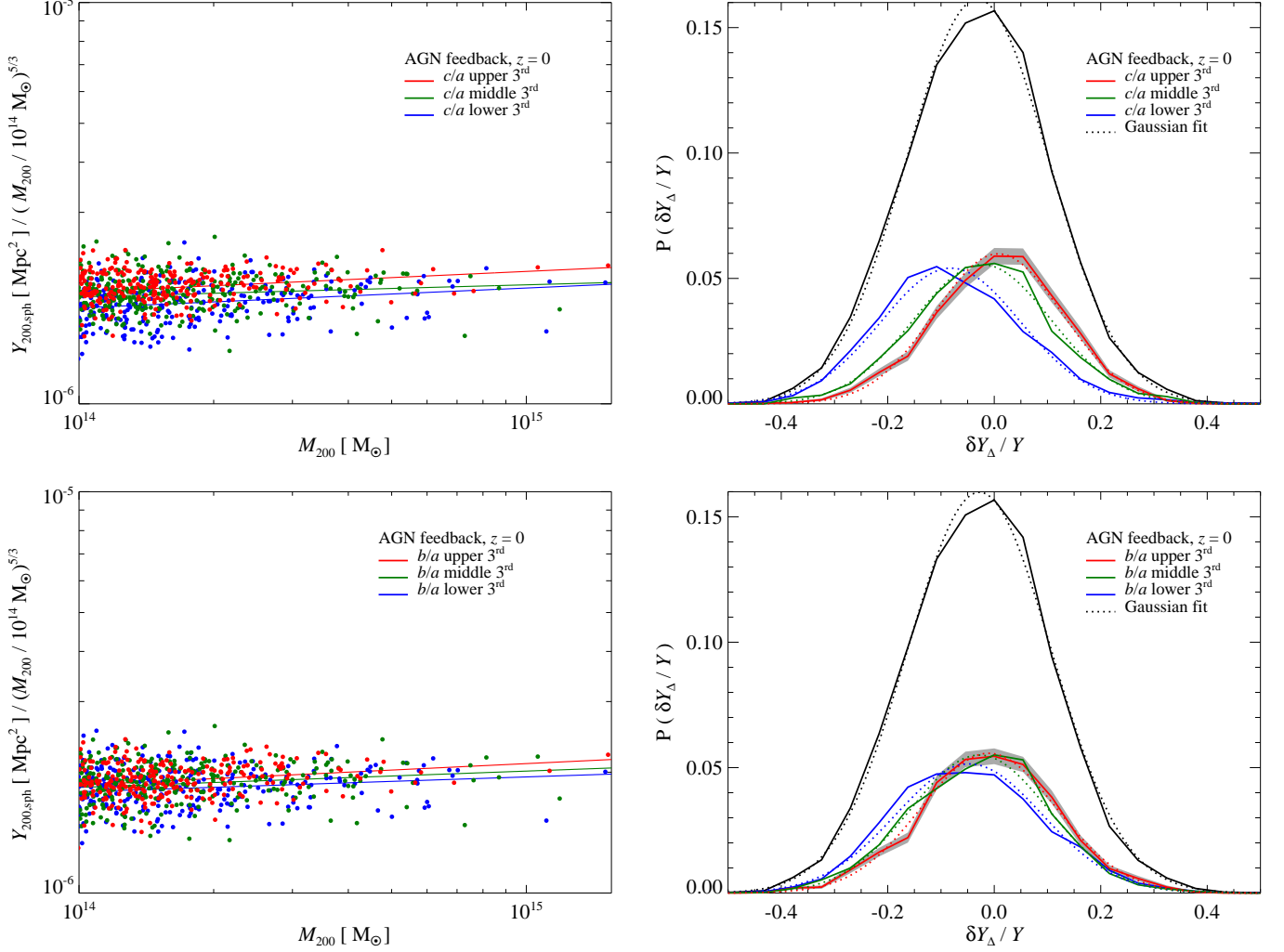
Figure 17. Sub-sampling the Y-M relations by the gas c/a axis ratio (upper panels) gas b/a axis ratio (lower panels) for the AGN simulations. Left: The Y-M scaling relation for the three c/a sub-samples, upper 3rd (red), middle 3rd (green) and lower 3rd (blue), with the corresponding slope fitted to those points. The y-axis has been scaled by $M^{5/3}$ to highlight the deviations from self-similarity. Right: The probability distributions for the relative deviation, $\delta Y_\Delta / Y$, with respect to the best fits for the three sub-samples and the total distribution (black), including the Gaussian fits (dotted lines) and the Poisson deviations for the upper 3rd sub-sample (grey band). The sub-sample of c/a containing the lowest values (largest ellipticities) shows systematically lower total Y values for a given mass and larger scatter, while the more spherical high c/a sub-sample shows a lower scatter of $\sim 12\%$. Additionally we find that the pressure c/a axis ratio sub-sample has similar results (cf. Table 2). The sub-sample of b/a containing the lowest values (largest projected ellipticities) shows larger scatter than the sub-sample with the highest values by $\sim 23\%$. There are significant changes in the Y-M relation at $z = 0$, however, smaller in comparison to the c/a sub-sampling.

moment-of-inertia tensor beyond R_{200}.

5.5. Toward a fundamental plane of Y-M

After quantifying the scatter of the entire sample, we aim at understanding its origin. This may enable us to either construct a linear combination of physically motivated observables that minimizes the scatter or to employ sub-sampling of the full distribution according to some parameter so that the resulting distribution exhibits a smaller intrinsic scatter and potentially allows for tighter cosmological constraints (e.g., Afshordi 2008).

In the previous sections we explored the average radial trends for kinetic pressure support from bulk motions and gas density/pressure shapes of the ICM. Utilizing this information, we rank order clusters according to their kinetic pressure support and intrinsic shape information. We follow the same fitting procedure as above for subsets of the lower 3rd, middle 3rd, and upper 3rd of the correspondingly sorted distributions in order

to demonstrate the impact of kinetic pressure support and asphericity on the Y-M relation fits and scatter. For the rest of this section we concentrate our analysis on the Y-M relations of the AGN feedback simulations, since they show the largest scatter (this will provide an upper limit on the scatter) and are most likely our best representation of "real" clusters in comparison to the other simulated physics models. We compute the ratio of kinetic-to-thermal energy, K/U, within radial bins and use this ratio as a measure of dynamical state for the galaxy clusters. We define the internal kinetic energy, K, and thermal energy, U, of a cluster as

$$K(< r) \equiv \sum_i \frac{3 m_{\mathrm{gas},i} P_{\mathrm{kin},i}}{2 \rho_i}, \qquad (16)$$

$$U(< r) \equiv \sum_i \frac{3 m_{\mathrm{gas},i} P_{\mathrm{th},i}}{2 \rho_i}, \qquad (17)$$
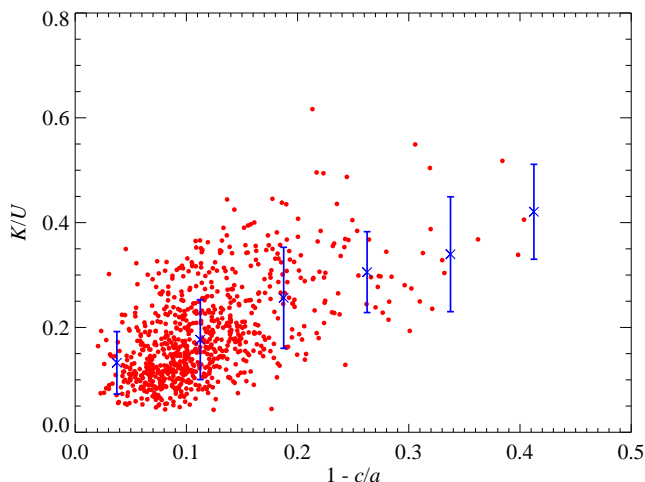
Figure 18. The correlations between the K/U ratio and $1 - c/a$. Here the red points represent each cluster in the simulations and the blue crosses are average quantities. The linear correlation coefficient is 0.575

where m and ρ are the gas mass and the SPH density, respectively for all particles i less than radius r. The ratio K/U is the volume integrated analog of the ratio P_{kin}/P_{th} shown in § 3 and hence is also an indicator of formation history and substructure. For the sub-sample with the highest ratio of K/U, we find a smaller normalization (cf. Fig. 16 and Table 2) where the difference between this upper 3rd of the distribution and lower 3rd is $\sim 15\%$. Here some of the thermal pressure support has been compensated for by kinetic pressure support resulting in lower integrated thermal electron pressure, thus, lowering Y-values. More massive clusters are typically in the high K/U sample rather then the other two samples. We find that the sub-sample with the smallest K/U values shows the lowest scatter, $\sim 11\%$ for the AGN feedback simulations. Further sub-sampling of the smallest K/U values (e.g., the lowest 6th) does not decrease the scatter, which is limited to $\sim 11\%$.

We also sort our cluster sample by the ratio of minor to major axis for both 3D and projected 2D, c/a and b/a[3] respectively, as defined in Sec. 4. Following the same procedure as for the K/U sub-sample and restricting ourselves to the AGN feedback simulations, we find that splitting the clusters up by ellipticity, c/a, gives similar results in comparison to K/U-splitting. The galaxy clusters with smaller ellipticities have larger total Y values and less scatter, while the more triaxial clusters have lower total Y and large scatter (cf. Fig. 17). These trends are reflected in the fit parameters of the sub-sample Y-M relation shown in Table 2, where the differences between the upper 3rd and lower 3rd sub-samples normalization parameters is $\sim 12\%$. Additionally, we found that using the pressure shapes instead of the gas shapes yield almost identical results (cf. Table 2). We find that sub-sampling the clusters with the b/a statistics has the greatest impact on the scatter. The sub-sample of clusters that appear to be elongated in the plane of the sky have larger scatter than the more spherical clusters (cf. Fig. 17 and Table 2). Also, the b/a sub-sampling causes a similar bias in the Y-M relation in comparison to the c/a sub-sampling, but not as significant.

The results from sub-sampling clusters according K/U and c/a indicate that there are correlations between these physical

---

[3] We show one projection for the b/a sub-sampling. The other projections yield similar results.

properties and the scatter in the Y-M relation. In Figure 18 we show that larger K/U ratios correlate with larger $1 - c/a$, i.e. larger triaxiality, with a linear coefficient value, $r_s = 0.58$. These correlations between kinetic pressure support and ellipticity are the result of the growth of structure being hierarchical. This supports the argument that kinetic pressure support, ellipticity and sub-structure are all tracers of the dynamical state and the formation history of galaxy clusters, which is the ultimate cause of the intrinsic scatter of the Y-M relation. Similar results were found by Rasia et al. (2011) and Krause et al. (2011) Previous work by Yang et al. (2010) found mass trends in the measured scatter, which is consistent with our findings after extrapolating their lower mass range to our larger masses. However, their conclusion is different from ours, since they claim that the scatter is most sensitive to the DM concentration; a finding that may partially be due to the insufficient resolution in their simulations.

6. DISCUSSION AND CONCLUSIONS

In this paper we demonstrate that the spatial distribution of the ICM, kinetic pressure support from bulk motions, and self-regulated thermal energy feedback in clusters cores (that we refer to as AGN feedback) all play very important roles for the thermal properties of galaxy clusters. In particular, the observables for large SZ cluster surveys, such as ACT, SPT and *Planck*, will be modified by these processes. Below we highlight and expand on our main results.

Non-thermal pressure support and cluster shapes: The contribution to the overall pressure support in clusters from bulk motions, P_{kin}, increases substantially for larger radii and is a strong function of both, cluster mass and redshift. Including AGN feedback marginally decreases P_{kin}/P_{th} in comparison to the other (more simplified) simulation models, namely our shock heating-only model and that which additionally includes radiative cooling, star formation, supernova feedback, and CRs. However, the difference is not substantial enough to be statistically inconsistent with the variance around the median of P_{kin}/P_{th}. The mass dependence and redshift evolution of P_{kin}/P_{th} is governed by P_{kin} and a direct result of the hierarchical growth of structure. Semi-analytic approaches are just beginning to model P_{kin}. The full dependence on radius, mass and redshift of this component is, by definition, self-consistently included in hydrodynamic simulations.

We find that the distribution of gas density and pressure are weak functions of the simulated physics models within R_{200} (excluding the cluster core) and that AGN feedback mildly modifies the average gas shapes. The cluster mass dependence of the ellipticity is more moderate in comparison to P_{kin}/P_{th}. The ellipticity is small within R_{500} with little redshift evolution. In combination with the comparably small non-thermal pressure support at these scales (which rises dramatically beyond this characteristic radius), the small clumping factor measured in our simulations (cf. BBPS4), and the small modification of our simulated cluster physics at these radii (in particular of our implementation of AGN feedback), this result is reassuring for X-ray observations of clusters which use R_{500} to characterize clusters with high-quality *Chandra* and *XMM Newton* observations. Hence, our analysis theoretically supports this choice of radius (which was initially motivated by the simulations in Evrard et al. (1996)) and justifies some of the main assumptions such as spherical symmetry and an almost radius-independent hydrostatic mass bias of $\sim 20-25\%$ when using a fair sample of clusters without morphological selection which

may be applicable for the future eROSITA sample.

We find substantial redshift evolution in different dynamical quantities, e.g., P_{kin}/P_{th}, the velocity anisotropy, and anisotropy parameters such as ellipticities. This is in particular the case for the changes in the power-law behaviors of the radial profile of these quantities such as the sudden break in ellipticities which moves to smaller radii as the redshift increases (when scaled to R_{200}). The break and the more pronounced ellipticities and P_{kin}/P_{th} outside a characteristic radius are a direct result of increased level of substructure predicted by hierarchical structure formation and the associated higher mass accretion rate at higher redshift. We explicitly show (in the Appendix C) that most of this redshift evolution is somewhat artificial and can be absorbed in a re-definition of the virial radius: scaling with the radius that contains a mean density of 200 times the average mass density rather than the critical density of the universe considerably weakens the observed trends with redshift. This also suggests a physical definition of the virial radius in terms of dynamical quantities (that, however, remain poorly defined observationally), e.g., the equipartition radius of thermal and kinetic pressure, the region where the velocity anisotropy becomes strongly radial, or the radius at which the ellipticity or substructure level increases dramatically. These seemingly different criteria all select a rather similar radius around $R_{200,m}$; almost independent of redshift.

On scales $> R_{500}$, stacking analyses of projected SZ cluster images can be done with data from SZ experiments such as ACT and SPT, and, provided there is a suitable sample size, one may be able to detect projected gas pressure shapes, potentially even in bins of redshift. The results on the randomly projected 2D axis ratios represent the theoretical expectations. Any statistics from the intrinsic 3D distribution is highly correlated with the projected 2D distribution; we find that the (more elliptical) intrinsic cluster shapes can on average be inferred from their projected analogues by applying a $\sim 5-10\%$ correction on the ellipticity. Another interesting outcome from our shape analysis is that there is no direct and simple mapping of shapes and alignments for DM spatial distribution to the gas and pressure distributions possible mostly due to the difference in substructure distribution and dissipational nature of the gas. This result is troublesome for semi-analytic models which use dissipationless simulations as a template to solve for the gas distributions and pressure shapes. Such a method will produce additional triaxiality and misalignment for such a semi-analytical model of the ICM. The overall magnitude of the shape is reconciled by using the gravitational potential (e.g., Ostriker et al. 2005; Bode et al. 2009; Trac et al. 2011) which has been shown to be less triaxial (Lau et al. 2011) than the DM. However, providing an algorithm to re-alignment these pseudo gas distributions is a non-trivial task.

Y-M scaling relations: Our simulations are in good agreement with the current Y-M scaling relations from both X-ray observations and SZ surveys. However, to properly predict the Y-M scaling relations for an SZ experiment such as ACT, SPT or *Planck* without any prior knowledge of cluster masses, careful mock observations are needed. Those would have to include a simulation of the CMB sky with associated experiment noise and adopt the relevant cluster selection pipelines for the given experiment that employs the same cluster profile used for matched filtering in order to include all the systematics and potential biases that are intrinsic to the data analysis, e.g., X-ray priors on the aperture size.

We find that the inclusion of AGN feedback causes a deviation from the predictions of self-similar evolution for both the normalization and slope of the Y-M relation (as measured within R_{200}). However, we recover the self-similar slope again in our projected Y-M scaling relations (where we integrate along a cylinder of half-height $3R_{200}$), suggesting that AGN feedback pushes a fraction of its gas beyond the virial radius and a larger aperture/projection radius is able to recover the thermal energy from this larger reservoir of gas.

Including AGN feedback also increases scatter in the Y-M relation compared to simulations that include shock heating alone, from $\sim 11\%$ to $\sim 13\%$. Interestingly, sorting the clusters into sub-samples of K/U and c/a will reduce this scatter; e.g., K/U sub-sampling reduces the scatter from $\sim 12\%$ to $\sim 11\%$. We find that sub-sampling introduces only a small (predictable) bias in the normalizations on the order of a few percent. This suggests that observational proxies for the dynamical state and ellipticities may be used to construct a fundamental plane of the Y-M relation. The scatter ultimately originates from the merging history with its redshift and mass dependent accretion rates; those determine the non-thermal pressure support, the level of substructure, and the ellipticity. While sub-sampling on one of these secondary tracers may decrease the scatter, it is unlikely to decrease much more if more tracers are used (as they probe the same underlying process, albeit with a different weighting). Conversely, our band-splitting analysis on the Y-M relations suggests that large outliers from the mean relations would be interesting candidates for follow up with high resolution SZ observations, since they are more likely to have larger kinetic pressure support and ellipticities.

A fundamental point to take away is that all results at larger radii ($> R_{200}$) for the kinetic pressure support and ICM shapes are dominated by substructure. We also see the impact of substructure on the cylindrical Y-M scaling relation when integrating along the major axis with which substructure is preferentially aligned. Quantifying substructure statistically is difficult because of the problem of double-counting: the large volume contained within the radius that contains 95% of the total SZ flux, $4R_{200}$, necessarily leads to overlapping volumes of neighboring clusters, especially at high-redshift. Thus, this property remains challenging to model phenomenologically or analytically.

As discussed previously in the literature (e.g. Battaglia et al. 2010; Sun et al. 2011) SZ galaxy cluster may provide further insight into the interesting astrophysics associated with the ICM of clusters. This however may significantly complicate cosmological analyses in producing competitive constraints. However, these are exciting prospects for studies of feedback and other energy injection processes within clusters especially at higher redshift since the selection function of SZ cluster surveys probes clusters which populate the massive and high redshift end of the distribution.

REFERENCES

Afshordi, N. 2008, ApJ, 686, 201
Agertz, O. et al. 2007, MNRAS, 380, 963
Allgood, B., Flores, R. A., Primack, J. R., Kravtsov, A. V., Wechsler, R. H., Faltenbacher, A., & Bullock, J. S. 2006, MNRAS, 367, 1781
Andersson, K. et al. 2010, arXiv:1006.3068
Arnaud, M., Pratt, G. W., Piffaretti, R., Böhringer, H., Croston, J. H., & Pointecouteau, E. 2010, A&A, 517, A92
Bardeen, J. M., Bond, J. R., Kaiser, N., & Szalay, A. S. 1986, ApJ, 304, 15
Battaglia, N., Bond, J. R., Pfrommer, C., & Sievers, J. L. 2011a, in prep.
—. 2011b, in prep.
—. 2011c, in prep.
Battaglia, N., Bond, J. R., Pfrommer, C., Sievers, J. L., & Sijacki, D. 2010, ApJ, 725, 91
Benson, B. A., Church, S. E., Ade, P. A. R., Bock, J. J., Ganga, K. M., Henson, C. N., & Thompson, K. L. 2004, ApJ, 617, 829
Birkinshaw, M. 1999, Phys. Rep., 310, 97
Bode, P., Ostriker, J. P., & Vikhlinin, A. 2009, ApJ, 700, 989
Bode, P., Ostriker, J. P., Weller, J., & Shaw, L. 2007, ApJ, 663, 139
Bonaldi, A., Tormen, G., Dolag, K., & Moscardini, L. 2007, MNRAS, 378, 1248
Bonamente, M., Joy, M., LaRoque, S. J., Carlstrom, J. E., Nagai, D., & Marrone, D. P. 2008, ApJ, 675, 106
Bond, J. R., & Myers, S. T. 1996, ApJS, 103, 1
Bryan, G. L., & Norman, M. L. 1998, ApJ, 495, 80
Burns, J. O., Skillman, S. W., & O'Shea, B. W. 2010, ApJ, 721, 1105
Carlstrom, J. E., Holder, G. P., & Reese, E. D. 2002, ARA&A, 40, 643
Cavagnolo, K. W., Donahue, M., Voit, G. M., & Sun, M. 2009, ApJS, 182, 12
Chaudhuri, A., & Majumdar, S. 2011, ApJ, 728, L41
Churazov, E., Brüggen, M., Kaiser, C. R., Böhringer, H., & Forman, W. 2001, ApJ, 554, 261
da Silva, A. C., Kay, S. T., Liddle, A. R., & Thomas, P. A. 2004, MNRAS, 348, 1401
Dubinski, J., & Carlberg, R. G. 1991, ApJ, 378, 496
Dunkley, J. et al. 2010, arXiv:1009.0866
Enßlin, T. A., Pfrommer, C., Springel, V., & Jubelgas, M. 2007, A&A, 473, 41
Ensslin, T. A., Simon, P., Biermann, P. L., Klein, U., Kohle, S., Kronberg, P. P., & Mack, K.-H. 2001, ApJ, 549, L39
Evrard, A. E. 1990, ApJ, 363, 349
Evrard, A. E., Metzler, C. A., & Navarro, J. F. 1996, ApJ, 469, 494
Fabian, A. C. 1994, ARA&A, 32, 277
Fabian, A. C., Sanders, J. S., Allen, S. W., Crawford, C. S., Iwasawa, K., Johnstone, R. M., Schmidt, R. W., & Taylor, G. B. 2003, MNRAS, 344, L43
Fowler, J. W. et al. 2010, arXiv:1001.2934
Frenk, C. S. et al. 1999, ApJ, 525, 554
Gottlöber, S., Klypin, A., & Kravtsov, A. V. 2001, ApJ, 546, 223
Gottlöber, S., & Yepes, G. 2007, ApJ, 664, 117
Huchra, J. P., & Geller, M. J. 1982, ApJ, 257, 423
Iapichino, L., & Niemeyer, J. C. 2008, MNRAS, 388, 1089
Jing, Y. P., & Suto, Y. 2002, ApJ, 574, 538
Jubelgas, M., Springel, V., Enßlin, T., & Pfrommer, C. 2008, A&A, 481, 33
Kaiser, N. 1986, MNRAS, 222, 323
Kasun, S. F., & Evrard, A. E. 2005, ApJ, 629, 781
Keisler, R. et al. 2011, arXiv:1105.3182
Komatsu, E., & Seljak, U. 2002, MNRAS, 336, 1256
Krause, E., Pierpaoli, E., Dolag, K., & Borgani, S. 2011, arXiv:1107.5740
Kravtsov, A. V., Vikhlinin, A., & Nagai, D. 2006, ApJ, 650, 128
Lau, E. T., Kravtsov, A. V., & Nagai, D. 2009, ApJ, 705, 1129
Lau, E. T., Nagai, D., Kravtsov, A. V., & Zentner, A. R. 2011, ApJ, 734, 93
Lewis, G. F., Babul, A., Katz, N., Quinn, T., Hernquist, L., & Weinberg, D. H. 2000, ApJ, 536, 623
Lima, M., & Hu, W. 2004, Phys. Rev. D, 70, 043504
Lueker, M. et al. 2010, ApJ, 719, 1045
Macciò, A. V., Dutton, A. A., & van den Bosch, F. C. 2008, MNRAS, 391, 1940
Majumdar, S., & Mohr, J. J. 2003, ApJ, 585, 603
—. 2004, ApJ, 613, 41
Marriage, T. A. et al. 2010, aXiv:1010.1065
Marrone, D. P. et al. 2011, arXiv:1107.5115
—. 2009, ApJ, 701, L114
McCarthy, I. G., Schaye, J., Bower, R. G., Ponman, T. J., Booth, C. M., Vecchia, C. D., & Springel, V. 2011, MNRAS, 412, 1965
McNamara, B. R., Nulsen, P. E. J., Wise, M. W., Rafferty, D. A., Carilli, C., Sarazin, C. L., & Blanton, E. L. 2005, Nature, 433, 45

Miniati, F., Ryu, D., Kang, H., Jones, T. W., Cen, R., & Ostriker, J. P. 2000, ApJ, 542, 608
Mitchell, N. L., McCarthy, I. G., Bower, R. G., Theuns, T., & Crain, R. A. 2009, MNRAS, 395, 180
Motl, P. M., Hallman, E. J., Burns, J. O., & Norman, M. L. 2005, ApJ, 623, L63
Mroczkowski, T. 2011, ApJ, 728, L35
Mroczkowski, T. et al. 2009, ApJ, 694, 1034
Nagai, D. 2006, ApJ, 650, 538
Nagai, D., & Lau, E. T. 2011, ApJ, 731, L10
Nath, B. B., & Majumdar, S. 2011, arXiv:1105.2826
Ostriker, J. P., Bode, P., & Babul, A. 2005, ApJ, 634, 964
Parrish, I. J., McCourt, M., Quataert, E., & Sharma, P. 2011, arXiv:1109.1285
Pearce, F. R., Thomas, P. A., Couchman, H. M. P., & Edge, A. C. 2000, MNRAS, 317, 1029
Pfrommer, C., Chang, P., & Broderick, A. E. 2011, arXiv:1106.5505
Pfrommer, C., Enßlin, T. A., Springel, V., Jubelgas, M., & Dolag, K. 2007, MNRAS, 378, 385
Pfrommer, C., & Jones, T. W. 2011, ApJ, 730, 22
Pfrommer, C., Springel, V., Enßlin, T. A., & Jubelgas, M. 2006a, MNRAS, 367, 113
—. 2006b, MNRAS, 367, 113
Pinzke, A., Pfrommer, C., & Bergstrom, L. 2011, arXiv:1105.3240
Planck Collaboration et al. 2011a, arXiv:1101.2026
—. 2011b, arXiv:1101.2024
—. 2011c, arXiv:1101.2043
Rasia, E., Mazzotta, P., Evrard, A., Markevitch, M., Dolag, K., & Meneghetti, M. 2011, ApJ, 729, 45
Rasia, E., Tormen, G., & Moscardini, L. 2004, MNRAS, 351, 237
Rudd, D. H., Zentner, A. R., & Kravtsov, A. V. 2008, ApJ, 672, 19
Ryu, D., Kang, H., Hallman, E., & Jones, T. W. 2003, ApJ, 593, 599
Sayers, J., Golwala, S. R., Ameglio, S., & Pierpaoli, E. 2011, ApJ, 728, 39
Schäfer, B. M., Pfrommer, C., Bartelmann, M., Springel, V., & Hernquist, L. 2006a, MNRAS, 370, 1309
Schäfer, B. M., Pfrommer, C., Hell, R. M., & Bartelmann, M. 2006b, MNRAS, 370, 1713
Sehgal, N. et al. 2011, ApJ, 732, 44
Shaw, L. D., Holder, G. P., & Bode, P. 2008, ApJ, 686, 206
Shaw, L. D., Nagai, D., Bhattacharya, S., & Lau, E. T. 2010, ApJ, 725, 1452
Shirokoff, E. et al. 2010, arXiv:1012.4788
Sijacki, D., Pfrommer, C., Springel, V., & Enßlin, T. A. 2008, MNRAS, 387, 1403
Sijacki, D., Springel, V., Di Matteo, T., & Hernquist, L. 2007, MNRAS, 380, 877
Simionescu, A. et al. 2011, Science, 331, 1576
Skillman, S. W., O'Shea, B. W., Hallman, E. J., Burns, J. O., & Norman, M. L. 2008, ApJ, 689, 1063
Springel, V. 2005, MNRAS, 364, 1105
—. 2010, MNRAS, 401, 791
Springel, V., & Hernquist, L. 2003, MNRAS, 339, 289
Springel, V. et al. 2008a, MNRAS, 391, 1685
—. 2008b, Nature, 456, 73
Stanek, R., Rasia, E., Evrard, A. E., Pearce, F., & Gazzola, L. 2010, ApJ, 715, 1508
Suginohara, T., & Ostriker, J. P. 1998, ApJ, 507, 16
Sun, M., Sehgal, N., Voit, G. M., Donahue, M., Jones, C., Forman, W., Vikhlinin, A., & Sarazin, C. 2011, ApJ, 727, L49
Sunyaev, R. A., & Zeldovich, Y. B. 1970, Ap&SS, 7, 3
Thompson, T. A., Quataert, E., & Murray, N. 2005, ApJ, 630, 167
Trac, H., Bode, P., & Ostriker, J. P. 2011, ApJ, 727, 94
Vanderlinde, K. et al. 2010, ApJ, 722, 1180
Vazza, F., Brunetti, G., & Gheller, C. 2009, MNRAS, 395, 1333
Vazza, F., Dolag, K., Ryu, D., Brunetti, G., Gheller, C., Kang, H., & Pfrommer, C. 2011, arXiv:1106.2159
Vogelsberger, M., Sijacki, D., Keres, D., Springel, V., & Hernquist, L. 2011, arXiv:1109.1281
Voit, G. M. 2005, Reviews of Modern Physics, 77, 207
Wechsler, R. H., Bullock, J. S., Primack, J. R., Kravtsov, A. V., & Dekel, A. 2002, ApJ, 568, 52
White, M. 2002, ApJS, 143, 241
Yang, H., Bhattacharya, S., & Ricker, P. M. 2010, ApJ, 725, 1124
Zemp, M., Gnedin, O. Y., Gnedin, N. Y., & Kravtsov, A. V. 2011, arXiv:1108.5384
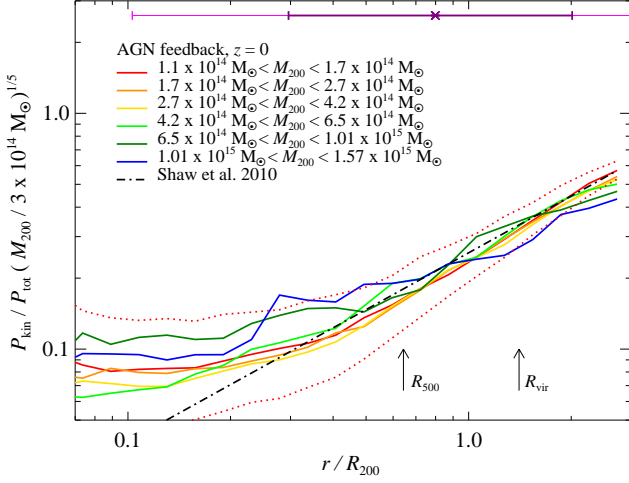Zhao, D. H., Jing, Y. P., Mo, H. J., & Börner, G. 2009, ApJ, 707, 354

Figure 19. The kinetic pressure-to-total pressure is weakly mass-dependent, $P_{kin}/P_{tot} \propto M_{200}^{1/5}$ as indicated by the scaling of the y-axis. Shown is the median of P_{kin}/P_{tot} as a function of radius for the AGN feedback simulations for various mass bins with the 25th and 75th percentile values illustrated by the dotted lines for the lowest mass bin at $z = 0$. For comparison, we also show the model for P_{kin}/P_{tot} by Shaw et al. (2010), which has been fit to match AMR simulations (dash-dotted). We illustrate the 1 and 2 σ contributions to Y_Δ centered on the median for the feedback simulation by horizontal purple and pink error bars. Therefore, ignoring this mass dependence results in a 60 % difference in this ratio for an order of magnitude change in the cluster mass. The median of P_{kin}/P_{th} scales as $M_{200}^{1/3}$, which results in a larger difference.
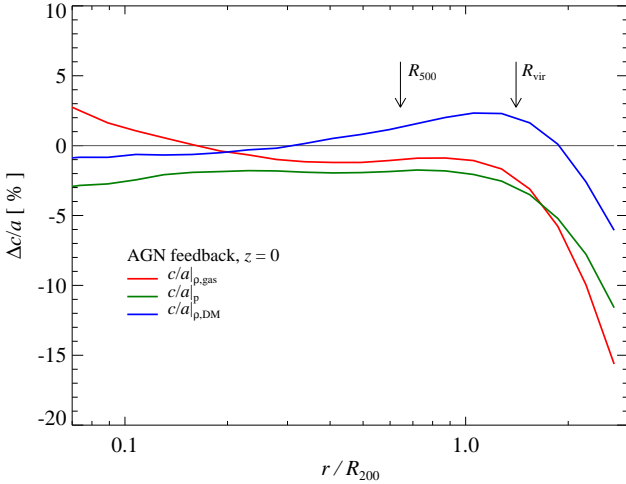

Figure 20. Shown is the relative difference between axis ratios with and without the r^{-2} weighting for the gas-density (red line), DM-density (blue line) and gas-pressure (green line) weightings. Additionally including the r^{-2} weighting in the definition of the moment-of-inertia tensor down-weights the contribution at larger radii by $\lesssim 15\%$, thus reducing the effect of substructure.

APPENDIX

A. FITTING FUNCTION FOR P_{KIN}/P_{TOT}

In Section 3 we show that the ratio P_{kin}/P_{th} is a function of mass. However, the previous empirical fitting function for P_{kin}/P_{tot} (Shaw et al. 2010) does not include a mass dependence,

$$\frac{P_{kin}}{P_{tot}}(r,z) = \alpha(z) \left(\frac{r}{R_{500}}\right)^{n_{nt}} \left(\frac{M_{200}}{3 \times 10^{14} M_\odot}\right)^{n_M}, \quad (A1)$$

where $\alpha(z) \equiv \alpha_0(1+z)^\beta$ for low redshifts ($z \lesssim 1$) and the fit parameters are $\alpha_0 = 0.18 \pm 0.06$, $\beta = 0.5$, $n_{nt} = 0.8 \pm 0.25$, and by construction, $n_M = 0$. In Fig. 19 we compare the fitting function for Eq. (A1) and P_{kin}/P_{tot}, split by different mass bin which have been scaled by $M_{200}^{1/5}$, i.e. $n_M = 1/5$, that minimizes our χ^2. We chose a normalization of $3 \times 10^{14} M_\odot$ to match the fitting function of Shaw et al. (2010). Thus, the median difference between P_{kin}/P_{tot} of a $10^{15} M_\odot$ and a $10^{14} M_\odot$ cluster is $\sim 60\%$. The ratio in Eq. (A1) is similar to what is shown Fig. 1, however, P_{kin}/P_{th} depends more sensitively on mass. We find that the mass dependence for this ratio amounts to $M_{200}^{1/3}$.

B. DOWN-WEIGHTING THE SUBSTRUCTURE IN THE MOMENT-OF-INERTIA TENSOR

For both the gas density- and pressure-weighting of the moment-of-inertia tensor, the inclusion of an additional x^{-2}-weighting has a relatively minor influence on cluster shapes (cf. Fig. 20) and we do not see large differences in the axis ratios at the larger radii. The x^{-2}-weighting does lessen the influence of substructure which we have seen to be important at radii beyond R_{200}, but it does not remove it or isolate its signal. This would be a non-trivial task for any stacking analysis as it was recently suggested by Zemp et al. (2011).

C. CLUSTERS IN VELOCITY SPACE AND A DYNAMICAL RADIUS DEFINITION

The radial trends over redshift seen in Figures 1 and 10 call for re-examination of the choice for the working definition of radius, which is directly related to the definition of the cluster mass (see White 2002, for a more thorough discussion of cluster mass definitions in dissipationless simulations). It has been the common choice by both observers and theorists to define the mass within an radii where the average overdensity is greater than a large multiple of a given background density, such as $\rho_{cr}(z)$ and $\bar{\rho}_m(z)$. For low redshift observations, the more popular definition has been the $\rho_{cr}(z)$ as the iso-density surface, since no prior knowledge of Ω_m is required. The question remains what definition is physically more intuitive when comparing across various redshifts. At late times ($z < 1$), clearly the inclusion of the dark energy greatly influences the redshift evolution of the critical density compared to the mean matter density. For a hypothetical isolated non-accreting cluster using the R_Δ definition will result in the cluster radius shrinking as time approaches present day. Using the $R_{\Delta,m}$ scaling we find that the radial regions at which kinetic pressure is in equipartition with thermal pressure and the sharp break found in the ICM ellipticity align at $\sim 200 R_{\Delta,m}$ (cf. Fig. 21). In BBPS3 we show that the velocity anisotropy has the same radial trends as in Figures 1 and 10 and that $200 R_{\Delta,m}$ traces a distinct dynamical region of clusters, the splash-back radius, i.e., is caused by the turn-around of earlier collapsed shells which minimizes the radial velocity component such that the tangential components dominate the velocity.

D. GAUSSIAN OR LOG-NORMAL SCATTER?

Previous approaches quantified the scatter around the best-fit Y-M scaling relation with a log-normal distribution, i.e. they characterized the distribution of $\delta \log Y_\Delta = \log Y_\Delta - \log Y_{\Delta,fit}$ with a Gaussian. Deviations from this log-normal distribution were computed with the Edgeworth expansion, introducing substantial higher order moments, such as skewness and kur-
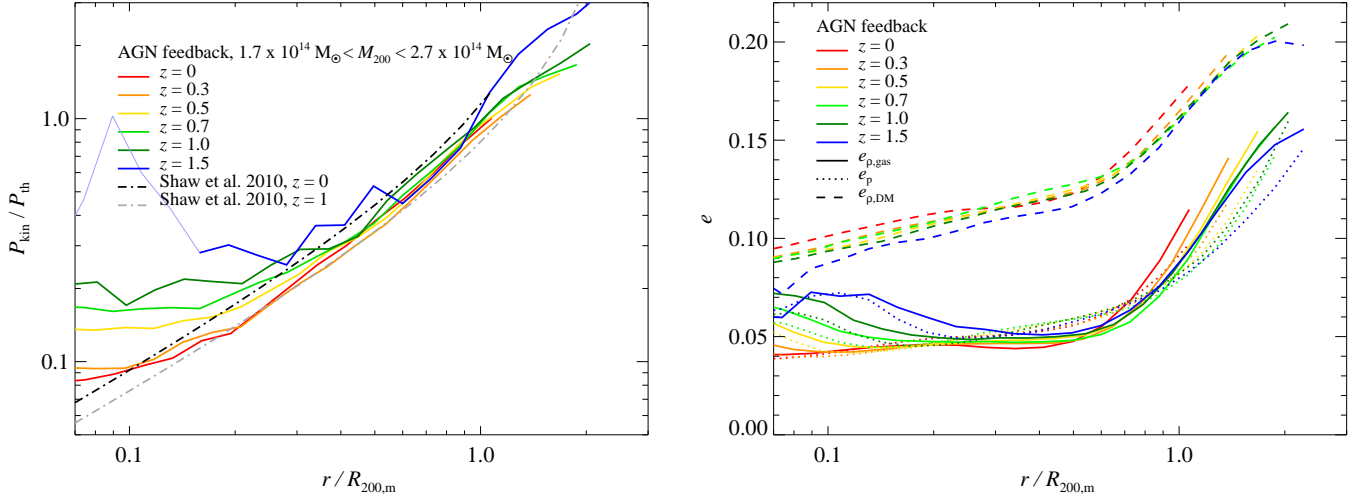
Figure 21. The choice for our working definition of virial radius has an impact on the redshift evolution of both, the kinetic pressure support (left) and ellipticity (right) of clusters. The figures shown here are the same as Fig. 1 and Fig. 10 except that the dimensionless radius has been scaled by $R_{200,m}$ instead of R_{200}. With this definition of virial radius, the redshift evolution of both, kinetic pressure support and ellipticity is weakened, especially in the outer regions.
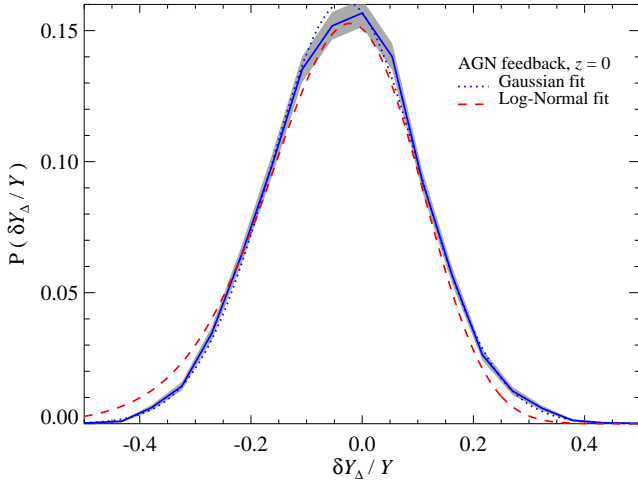

Figure 22. Comparison of Gaussian and log-normal scatter relative to the best-fit Y-M scaling relation at $z = 0$. We show the distribution of the relative *linear* deviation from the mean relation $\delta Y_\Delta / Y$ (cf. Eq. 15) with the solid blue line and compare it to a Gaussian fit (blue dotted line) and log-normal fit ($\delta \log Y_\Delta$, red dashed line). The Poisson deviations are shown with the grey band. Here we transformed the fit to the $\delta \log Y_\Delta$ distribution into $\delta Y_\Delta / Y$ so they could be shown together. The $\delta Y_\Delta / Y$ distribution is fit by a Gaussian better than the $\delta \log Y_\Delta$ distribution, with $\chi^2(\delta Y_\Delta / Y) \sim 1$ and $\chi^2(\delta \log Y_\Delta) \sim 7$. Forcing a log-normal distribution introduces higher-order moments such as skewness and kurtosis as can be seen by the asymmetric shapes of the tails in the log-normal fit.

tosis (e.g., Yang et al. 2010). Using a non-linear least squares approach we fit a Gaussian to both the $\delta \log Y_\Delta$ and $\delta Y_\Delta / Y$ distributions. In Fig. 22 we show that $\delta Y_\Delta / Y$ distribution is a better fit by a Gaussian within the (Poisson) uncertainties than the $\delta \log Y_\Delta$ distribution, with $\chi^2 \sim 1$ compared to $\chi^2 \sim 7$, respectively. Hence we suggest to use relative *linear* deviation instead of log-normal scatter for future characterizations of the scatter in Y-M relation.